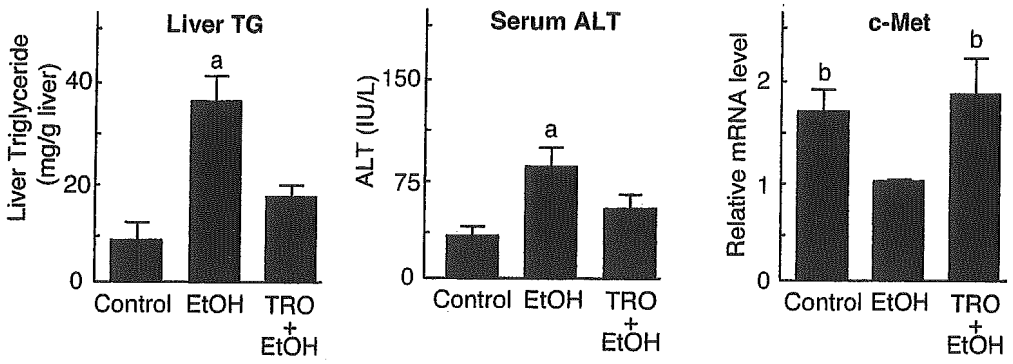

Figure 4. Troglitazone mimicked the actions of pioglitazone in vivo. Eight-week-old male SD rats fed ethanol-containing liquid diet were given troglitazone (200 mg/kg body weight per day) once every 24 hours intragastrically for 6 weeks. In this study, we divided the rats into 3 groups in the same way as our last examination of pioglitazone (n = 6). Troglitazone decreased accumulation of lipid droplets and suppressed the elevation of serum concentrations of ALT in ethanol-fed rats. Real-time PCR analyses showed that ethanol administration decreased hepatic c-Met expression and that troglitazone prevented this decrease. Results (and standard error of the mean) from 6 rats/group at the end of feeding period. All real-time quantitative PCR reactions were carried out in duplicate. $^{a}P < 0.05$ versus the other groups. $^{b}P < 0.05$ versus the ethanol-fed group. Control, rats pair-fed isocaloric liquid diet without ethanol; EtOH, ethanol-fed rats; TRO+EtOH, ethanol-fed rats given troglitazone.

not obese despite a high total energy intake.[23] Pioglitazone prevented the decrease in amount of adipose tissue, probably by mobilizing fat from the liver to adipose tissue.

It has been believed until now that impaired mitochondrial β-oxidation of fatty acids could be a major cause of triglyceride accumulation in alcoholic fatty liver.[24] In the current study, however, pioglitazone did not alter the expression of hepatic enzymes contributing to fatty acid oxidation such as carnitine palmitoyltransferase-1 or acyl-CoA oxidase (AOX) or the expression of hepatic TNF-α, uncoupling protein-2, PPARγ, or AMPK-catalytic subunit (α1 and α2) levels; plasma TNF-α, glucose, leptin, insulin levels, or insulin resistance remained unchanged. These results suggest that other mechanisms play central roles in pioglitazone's effect on alcoholic fatty liver. Differential

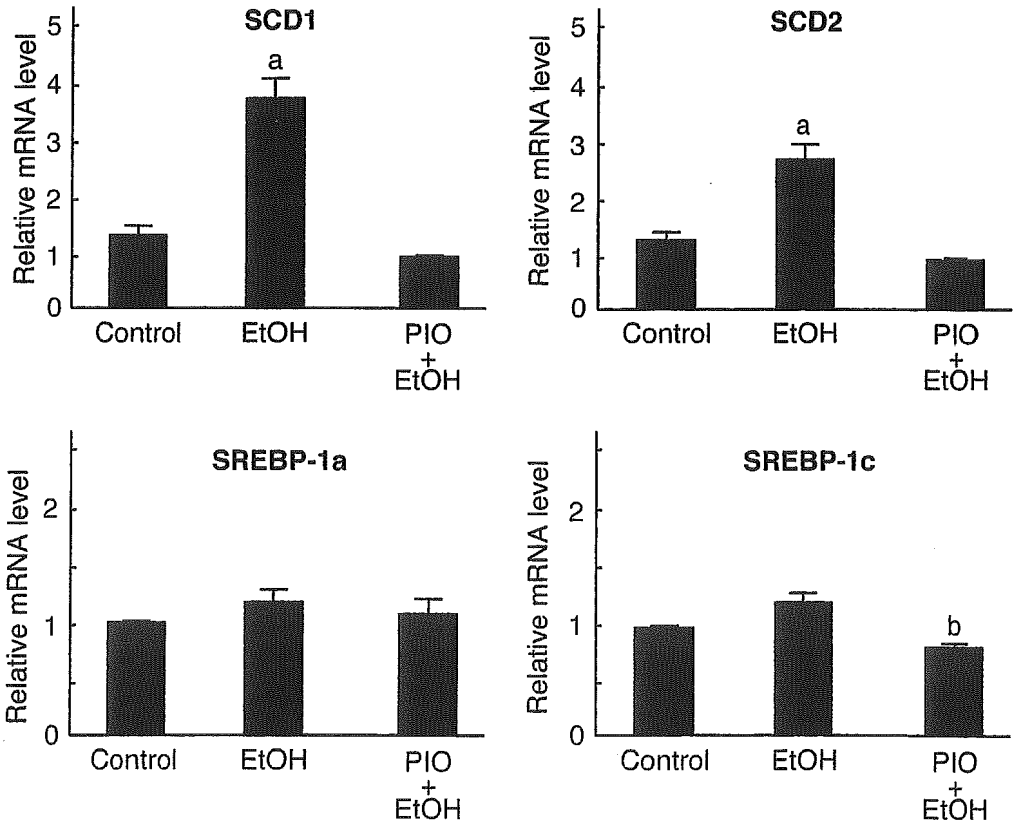

Figure 5. Hepatic SCD1, SCD2, SREBP-1a, and SREBP-1c expression. Real-time PCR analysis was carried out to quantitate hepatic mRNA levels of SCD1, SCD2, SREBP-1a, and SREBP-1c in liver homogenates among the groups. Results (and standard error of the mean) from 4 rats/group at the end of feeding period. All real-time quantitative PCR reactions were carried out in duplicate. $^{a}P < 0.05$ versus the other groups. $^{b}P < 0.05$ versus the ethanol-fed group. Control, rats pair-fed isocaloric liquid diet without ethanol; EtOH, ethanol-fed rats; PIO+EtOH, ethanol-fed rats given pioglitazone.

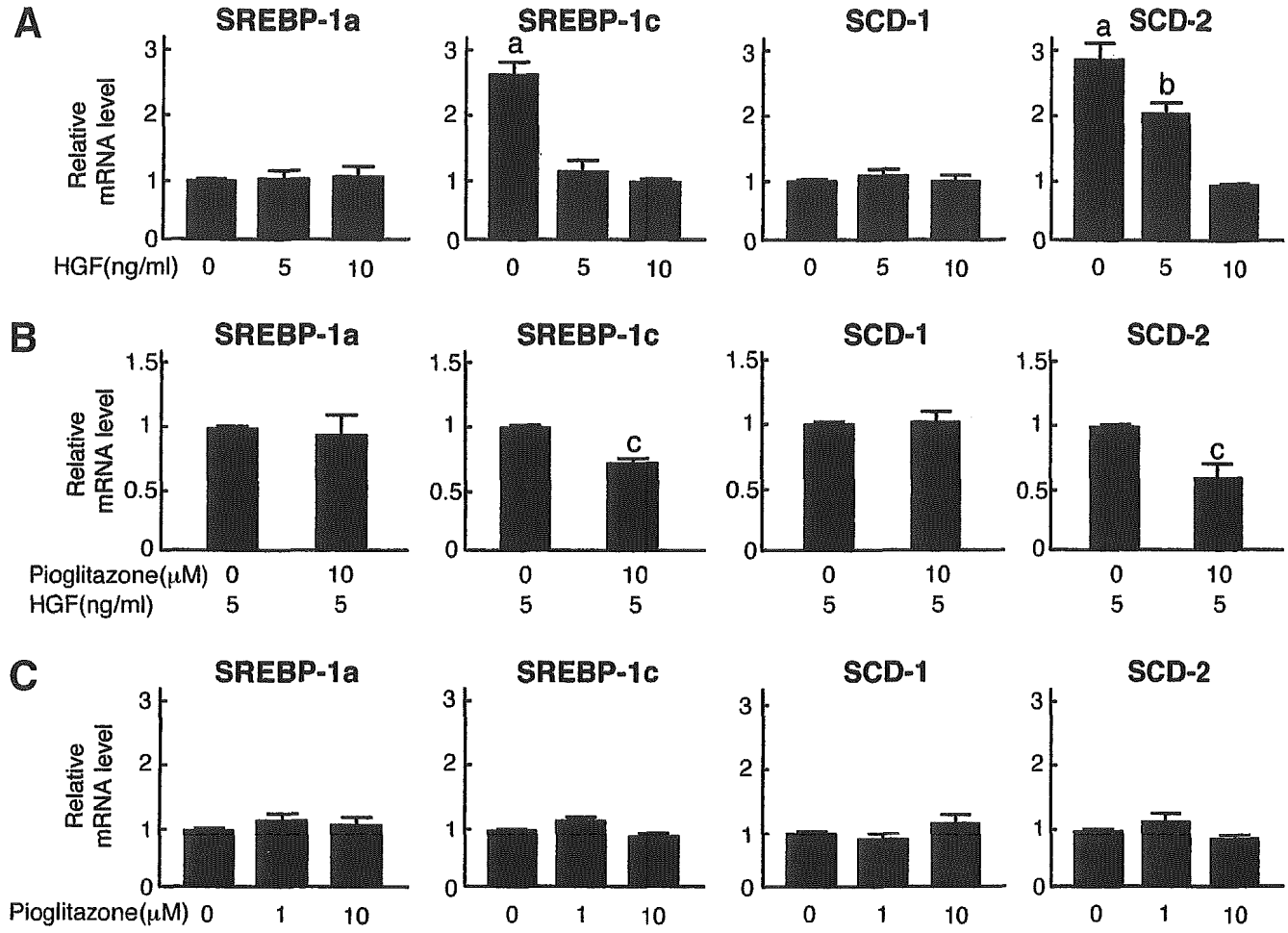

Figure 6. Effects of pioglitazone and HGF on expression of SREBP-1a, c, and SCD-1, 2 mRNA in hepatocyte cultures. Real-time PCR analysis was used to assess SREBP-1a, SREBP-1c, SCD-1, and SCD-2 gene expression. (*A*) Rat primary-cultured hepatocytes were incubated with various doses of HGF for 24 hours. $^{a}P < 0.05$ versus the other groups. $^{b}P < 0.05$ versus the group with addition of 10 ng/mL of HGF. (*B*) Incubation with pioglitazone with addition of 5 ng/mL of HGF for 24 hours. $^{c}P < 0.05$ versus the group without any addition of pioglitazone. (*C*) Incubation with various doses of pioglitazone for 24 hours. All real-time quantitative PCR reactions were carried out in duplicate. Results (and standard error of the mean) from 4 individual experiments.

transcriptome analyses comparing mRNA expression in the chronic ethanol-exposed livers with and without the pioglitazone treatment led us to pinpoint a critical role of the hepatic c-Met signaling pathway, and the results suggest that the reagent facilitates HGF-induced intracellular signaling without altering hepatic HGF levels.

HGF is the most potent stimulator of hepatocyte proliferation.[25] HGF has multiple biological properties in the liver, including mitogenic, antifibrotic, antiapoptotic, and cytoprotective activities.[26–28] Such multiple biological responses elicited by HGF are transferred through the cytoplasmic domain of c-Met, a specific cell surface transmembrane tyrosine kinase receptor.[26] Observation that pioglitazone directly enhanced both c-Met and its activated form in rat primary-cultured hepatocytes from ethanol-fed rats suggests that this reagent serves as the first clinically available tool that directly up-regulates c-Met expression in hepatocytes. Several data in the current study suggested that PPARγ is involved in mechanisms by which the reagent up-regulates c-Met, inasmuch as this event is mimicked by troglitazone, another PPARγ ligand, and is canceled by BADGE, a PPARγa antagonist. Further studies are necessary to determine the whole mechanisms for exploring direct actions of the reagent on c-Met expression.

HGF is known to stimulate apoB secretion in hepatocytes and to induce cell maturation during liver regeneration.[29] The HGF administration has recently been shown to improve alcoholic fatty liver by enhancing apoB synthesis and subsequent mobilization of lipids from hepatocytes with fatty changes.[13] These observations led us to examine if pioglitazone could serve as a

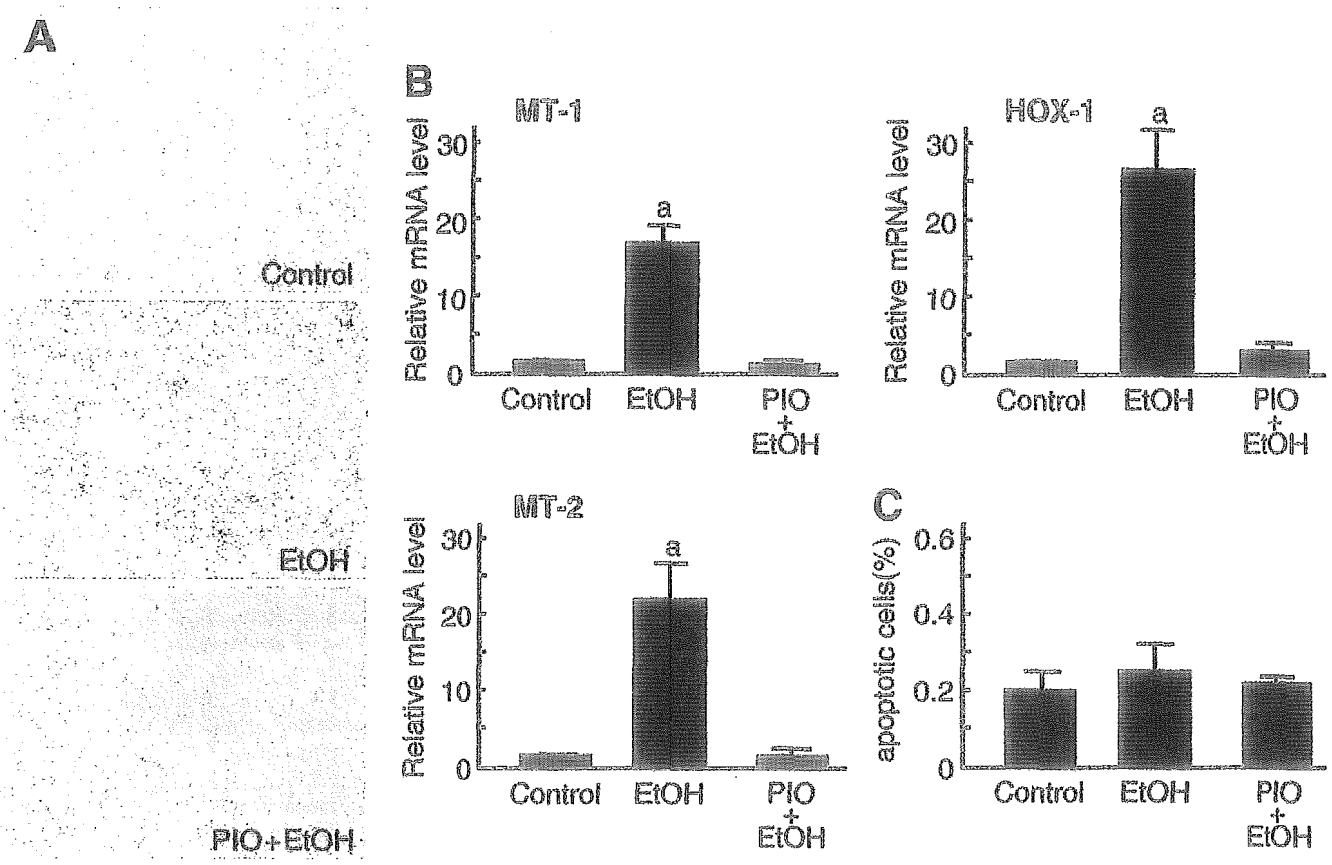

Figure 7. Effect of pioglitazone on hepatic lipid peroxidation, apoptosis, and expression of stress response proteins. (*A*) Immunohistochemistry for 4-HNE. Representative liver samples of control rat (Cont), ethanol-fed rats (EtOH), and ethanol-fed rats given pioglitazone (EtOH+Piog) (×100). (*B*) Real-time PCR analysis was used to assess stress response proteins such as MT-1, MT-2, and HOX-1 mRNA expression in liver homogenates among the groups. Results (and standard error of the mean) from 4 rats/group at the end of feeding period. All real-time quantitative PCR reactions were carried out in duplicate. $^{a}P < 0.05$ versus the other groups. (*C*) TUNEL results of liver apoptosis among the treated groups. The apoptotic cells and hepatocytes were counted from 5 lower microscopic fields for each animal.

substitute reagent that triggers lipid mobilization from the liver through stimulation of the c-Met pathway. As one might expect, the current results showed that pioglitazone mimics such effects of HGF to stimulate hepatic apoB synthesis and resultant VLDL secretion through HGF/c-Met intracellular signaling; this event could greatly contribute to mobilization of triglycerides from the liver undergoing chronic ethanol exposure.

Table 4. Blood Concentration of Ethanol and Acetaldehyde in Pioglitazone-Treated and Control Rats After Ethanol Administration (4 g/kg)

		Control	Pioglitazone Treated
Ethanol (mg/dL)	0 h	0 ± 0	0 ± 0
	2 h	184 ± 27	198 ± 26
	12 h	82 ± 22	84 ± 35
	24 h	3 ± 1	4 ± 2
Acetaldehyde (mg/L)	0 h	0 ± 0	0 ± 0
	2 h	1.9 ± 0.5	2.0 ± 0.4
	12 h	0.2 ± 0.1	0.2 ± 0.1
	24 h	0 ± 0	0 ± 0

Besides its action on lipid mobilization from the liver, pioglitazone obviously exerts its anti-steatotic actions through multiple mechanisms as judged by alterations in expression of genes responsible for triglyceride synthesis. SREBPs and stearoyl-CoA (SCD) are such genes responding to pioglitazone. Ntambi et al.[30] recently reported that a lipogenic diet fed to mice with a null mutation in the SCD1 gene (SCD1-/-) failed to induce the synthesis of triglycerides in liver, despite the induction of expression of SREBP-1 and its target genes. Cohen et al.[31] also reported that SCD-1 is required for the fully developed obese phenotype of leptin-deficient mice, including fatty liver. SCD-1 and SCD-2 catalyze the same reaction, and SCD-2 is reported to be expressed at higher levels in livers of mice overexpressing the truncated nuclear form of SREBP-1.[32] These observations suggest that induction of triglyceride synthesis is highly dependent on SCD

gene expression and that both SCD-1 and SCD-2 play a role in the mechanism of fatty liver. As shown in results from our and other laboratories, chronic ethanol feeding increased levels of SCD-2, and SREBP-1c expression. Consistent with our results, Crabb et al.[33] recently reported that chronic ethanol feeding activates hepatic SREBP-1. Such suppressive actions of pioglitazone on up-regulation of these genes could greatly improve ethanol-induced hepatic steatosis cooperatively with its aforementioned effects on the lipid mobilization via VLDL as a whole.

Recently, HGF was reported to prevent LPS-induced hepatic sinusoidal endothelial cell injury and intrasinusoidal fibrin deposition in rats.[34] It has also been reported that the mere presence of fat in the liver leads to hepatic lipid peroxidation and that chronic steatosis is associated with persistent lipid peroxidation.[35] Lipid peroxidation is proposed as a mechanism of alcohol-induced hepatotoxicity. It has been suggested that chronic lipid peroxidation could represent the missing link between chronic steatosis and steatohepatitis. In our study, pioglitazone improved ethanol-induced lipid peroxidation and resultant cellular damages by increasing the c-Met expression and by decreasing hepatic fat amounts, as indicated by results showing suppression of antioxidative genes such as MT-1, -2, and HOX-1.[36,37] Furthermore, so far as judged from the current TUNEL analyses, pioglitazone treatment did not induce any notable apoptosis in liver. Such a cytoprotective feature of pioglitazone on ethanol-induced hepatic steatosis is likely to be of great clinical advantage in that other thiazolidinedione derivatives such as troglitazone have been reported to induce apoptotic hepatocyte death, leading to a conflict for its clinical use.[38] Based on these findings, we propose an important new mechanism to explain the recovery from alcoholic fatty liver in response to pioglitazone (i.e., that pioglitazone enhances c-Met expression in hepatocytes, resulting in activation of HGF/c-Met signaling). The HGF/c-Met signaling activation induced by pioglitazone leads to increased apoB synthesis with subsequent lipid mobilization of VLDL from hepatocytes, and decreases hepatic SCD levels with decreased synthesis of triglycerides in liver. Such an effect of pioglitazone could also stimulate regeneration and attenuate lipid peroxidation.

The current study suggesting usefulness of pioglitazone to treat ethanol-induced hepatic steatosis led us to hypothesize that such an HGF-mimicking hepatoprotective PPARγ ligand could clinically be used to limit fatty infiltration of the liver caused by other disease conditions. For instance, posttransplant fatty infiltration in the donor liver accounts for a serious complication causing primary nonfunction.[39] Because use of steatotic livers are actually increasing for transplantation because of a shortage of the nonsteatotic donor grafts, we should find the method for amelioration of injury in donor fatty liver at liver transplantation. A possible use of the pioglitazone treatment deserves future studies if its use for posttransplanted recipients or for nonalcoholic steatohepatitis turned out to reduce the related liver injury. This may provide a means for designing future therapeutic strategies with pioglitazone. Pioglitazone may thus be useful as a therapeutic agent for alcoholic fatty liver and merits further evaluation.

References

1. Sorensen TI, Orholm M, Bentsen KD, Hoybye G, Eghoje K, Christoffersen P. Prospective evaluation of alcohol abuse and alcoholic liver injury in men as predictors of development of cirrhosis. Lancet 1984;2:241–4.
2. Teli MR, Day CP, Burt AD, Bennett MK, James OFW. Determinants of progression to cirrhosis or fibrosis in pure alcoholic fatty liver. Lancet 1995;346:987–990.
3. Lin HA, Yang SQ, Chuckaree C, Kuhajda F, Ronnet G, Diehl AM. Metformin reverses fatty liver disease in obese, leptin-deficient mice. Nat Med 2000;6:998–1003.
4. Zhou G, Myers R, Li Y, Chen Y, Shen X, Fenyk-Melody J, Wu M, Ventre J, Doebber T, Fujii N, Musi N, Hirshman MF, Goodyear LJ, Moller DE. Role of AMP-activated protein kinase in mechanism of metformin action. J Clin Invest 2001;108:1167–1174.
5. Shimabukuro M, Zhou YT, Lee Y, Unger RH. Troglitazone lowers islet fat and restores beta cell function of Zucker Diabetic Fatty rats. J Biol Chem 1998;273:3547–3550.
6. Higa M, Zhou YT, Ravazzola M, Baetens D, Orci L, Unger RH. Troglitazone prevents mitochondrial alterations, β cell destruction, and diabetes in obese prediabetic rats. Proc Natl Acad Sci U S A 1999;96:11513–11518.
7. Kakuma T, Lee Y, Higa M, Wang ZW, Pan W, Shimomura I, Unger RH. Leptin, troglitazone, and the expression of sterol regulatory element binding proteins in liver and pancreatic islets. Proc Natl Acad Sci U S A 2000;97:8536–8541.
8. Scheen AJ. Hepatotoxicity with thiazolidinediones: is it a class effect? Drug Saf 2001;24:873–888.
9. Lieber CS, DeCarli LM, Sorrell MF. Experimental methods of ethanol administration. Hepatology 1989;10:501–510.
10. Maeshida Y, Kiyota Y, Yoshimura Y, Motohashi M, Tanayama S. Disposition of the new antidiabetic agent pioglitazone in rats, dogs, and monkeys. Arzneim.-Forsch/Drug Res 1997;47:29–35.
11. Hayakawa T, Shiraki T, Morimoto T, Shii K, Ikeda H. Pioglitazone improves insulin signaling defects in skeletal muscle from Wistar fatty (fa/fa) rats. Biochem Biophys Res Commun 1996;223:439–444.
12. Horikoshi H, Yoshioka T, Kawasaki T, Nakamura K, Matsunuma N, Yamaguchi K, Sasahara K. Troglitazone (CS-045), a new antidiabetic drug. Annu Rep Sankyo Res Lab 1994;46:1–57.
13. Tahara M, Matsumoto K, Nukiwa T, Nakamura T. Hepatocyte growth factor leads to recovery from alcohol-induced fatty liver in rats. J Clin Invest 1999;103:313–320.
14. Bachorik PS, Ross JW. National cholesterol education program recommendations for measurement of low-density lipoprotein cholesterol: executive summary. Clin Chem 1995;41:1414–1420.

15. Hatch FT, Lees RS. Practical methods for plasma lipoprotein analysis. Adv Lipid Res 1968;6:1–68.
16. Tomita K, Sato M, Kajiwara K, Tanaka M, Tamiya G, Makino S, Tomizawa M, Mizutani A, Kuwano Y, Shiina T, Ishii H, Kimura M. Gene structure and promoter for *Crad2* encoding mouse cis-retinol/3α-hydroxysterol short-chain dehydrogenase isozyme. Gene 2000;251:175–186.
17. Dunn JCY, Yarmush ML, Koebe HG, Tompkins RG. Hepatocyte function and extracellular matrix geometry: long-term culture in a sandwich configuration. FASEB J 1989;3:174–177.
18. Lawrence JM, Reckless JP. Actos (pioglitazone): a new treatment for type 2 diabetes. Hosp Med 2001;62:411–416.
19. Pelizzari CA, Khodarev NN, Gupta N, Calvin DP, Weichselbaum RR. Quantitative analysis of DNA array autoradiographs. Nucleic Acids Res 2000;28:4577–4581.
20. Tenenbaum SA, Carson CC, Lager PJ, Keene JD. Identifying mRNA subsets in messenger ribonucleoprotein complexes by using cDNA arrays. Proc Natl Acad Sci U S A 2000;97:14085–14090.
21. Okada T, Mizoi Y. Studies on the problem of blood acetaldehyde determination in man and level after alcohol intake. Jpn J Alcohol Drug Depend 1982;17:141–159.
22. Wright HM, Clish CB, Mikami T, Hauser S, Yanagi K, Hiramatsu R, Serhan CN, Spiegelman BM. A synthetic antagonist for the peroxisome proliferator-activated receptor gamma inhibits adipocyte differentiation. J Biol Chem 2000;275:1873–1877.
23. Levine JA, Harris MM, Morgan MY. Energy expenditure in chronic abuse. Eur J Clin Invest 2000;30:779–786.
24. Eaton S, Record CO, Bartlett K. Multiple biochemical effects in the pathogenesis of alcoholic fatty liver. Eur J Clin Invest 1997;27:719–722.
25. Michalopoulos GK, Defrances MC. Liver regeneration. Science 1997;276:60–66.
26. Stuart KA, Riordan SM, Lidder S, Crostella L, Williams R, Skouteris GG. Hepatocyte growth factor/scatter factor-induced intracellular signaling. Int J Exp Pathol 2000;81:17–30.
27. Takehara T, Nakamura T. Protective effect of hepatocyte growth factor on *in vitro* hepatitis in primary cultured hepatocytes. Biomed Res 1991;12:335–338.
28. Ishiki Y, Ohnishi H, Muto Y, Matsumoto K, Nakamura T. Direct evidence that hepatocyte growth factor is a hepatotropic factor for liver regeneration and has a potent antihepatitis effect in vivo. Hepatology 1992;16:1227–1235.
29. Kaibori M, Kwon AH, Oda M, Kamiyama Y, Kitamura N, Okumura T. Hepatocyte growth factor stimulates synthesis of lipids and secretion of lipoproteins in rat hepatocytes. Hepatology 1998;27:1354–1361.
30. Ntambi JM, Miyazaki M, Stoehr JP, Lan H, Kendziorski CM, Yandell BS, Song Y, Cohen P, Friedman JM, Attie AD. Loss of stearoyl-CoA desaturase-1 function protects mice against adiposity. Proc Natl Acad Sci U S A 2002;99:11482–11486.
31. Cohen P, Miyazaki M, Socci ND, Hagge-Greenberg A, Liedtke W, Soukas AA, Sharma R, Hudgins LC, Ntambi JM, Friedman JM. Role for stearoyl-CoA desaturase-1 in leptin-mediated weight loss. Science 2002;297:240–243.
32. Shimomura I, Shimano H, Korn BS, Bashmakov Y, Horton JD. Nuclear sterol regulatory element-binding proteins activate genes responsible for the entire program of unsaturated fatty acid biosynthesis in transgenic mouse liver. J Biol Chem 1998;273:35299–35306.
33. You M, Fischer M, Deeg MA, Crabb DW. Ethanol induces fatty acid synthesis pathways by activation of sterol regulatory element-binding protein (SREBP). J Biol Chem 2002;277:29342–29347.
34. Sato S, Kaido T, Yamaoka S, Yoshikawa A, Arii S, Nakamura T, Niwano M, Imamura M. Hepatocyte growth factor prevents lipopolysaccharide-induced hepatic sinusoidal endothelial cell injury and intrasinusoidal fibrin deposition in rats. J Surg Res 1998;80:194–199.
35. Letteron P, Fromenty B, Terris B, Degott C, Pessayre D. Acute and chronic hepatic steatosis lead to in vivo lipid peroxidation in mice. J Hepatol 1996;24:200–208.
36. Kyokane T, Norimizu S, Taniai H, Yamaguchi T, Takeoka S, Tsuchida E, Naito M, Nimura Y, Ishimura Y, Suematsu M. Carbon monoxide from heme catabolism protects against hepatobiliary dysfunction in endotoxin-treated rat liver. Gastroenterology 2001;120:1227–1240.
37. Hayashi S, Takamiya R, Yamaguchi T, Matsumoto K, Tojo SJ, Tamatani T, Kitajima M, Makino N, Ishimura Y, Suematsu M. Induction of heme oxygenase-1 suppresses venular leukocyte adhesion elicited by oxidative stress: role of bilirubin generated by the enzyme. Circ Res 1999;85:663–671.
38. Yamamoto Y, Nakajima M, Yamazaki H, Yokoi T. Cytotoxicity and apoptosis produced by troglitazone in human hepatoma cells. Life Sci 2001;70:471–482.
39. Imber CJ, Peter SDS, Handa A, Friend PJ. Hepatic steatosis and its relationship to transplantation. Liver Transpl 2002;8:415–423.

Received March 8, 2003. Accepted December 4, 2003.

Address reprint requests to: Hiromasa Ishii, M.D., Department of Internal Medicine, School of Medicine, Keio University, 35 Shinanomachi, Shinjuku-ku, Tokyo 160-8582, Japan. e-mail: hishii@sc.itc.keio.ac.jp; fax: (81) 3-3356-9654.

Supported by a grant from Keio University, School of Medicine, Nateglinide Memorial Toyoshima Research and Education Fund, and the 21st Century Center-Of-Excellence (COE) Program from Ministry of Education, Culture, Sports, Science, and Technology.

The authors thank T. Saito, H. Ochiai, M. Tomizawa, and E. Tokubo for technical assistance.

Arch Histol Cytol, 66 (2): 155-162 (2003)

Expression of heme oxygenase-1 in rat ontogeny*

Takaoki Watanabe[1,2], Go Hasegawa[1], Takashi Yamamoto[1], Katsuyoshi Hatakeyama[2], Makoto Suematsu[3], and Makoto Naito[1]

[1]Division of Cellular and Molecular Pathology, [2]Division of Digestive and General Surgery, Niigata University Graduate School of Medical and Dental Sciences, Niigata; and [3]Department of Biochemistry, School of Medicine, Keio University, Tokyo, Japan

Summary. Heme oxygenase (HO), the heme-degrading enzyme, plays an important role in heme catabolism. Among three isozymes, HO-1 is an inducible form expressed mainly in macrophages. In rat ontogeny, HO-1 immunoreactivity was detected in mononuclear cells in the yolk sac at 10 days of gestation. HO-1-expressing cells were then detected in the fetal liver and their numbers increased during the gestational period. The numbers of HO-1-positive cells and HO-1 mRNA levels in the liver peaked at 18 days of gestation. Most of the macrophages expressed both HO-1 and a macrophage scavenger receptor. Macrophages in the fetal liver showed marked hemophagocytosis. Macrophages in the lung, spleen, bone marrow, and other tissues also expressed HO-1. HO-1 immunoreactivity was also observed in syncytial cells of the chorionic villi, the endodermal layer of the yolk sac, and renal tubules of the fetus. Intestinal mucosal epithelial cells expressed HO-1 after birth. These findings imply that HO-1 is crucial for macrophages in heme catabolism from an early stage of ontogeny. HO-1 expression in non-macrophagic cells may be required for other purposes such as protection from oxidative stress and various stimuli.

Received January 17, 2003

* This work was supported in part by Grants-in-Aid for Scientific Research from the Ministry of Education, Science, and Culture of Japan, and Japan Foundation Grant for Aging and Health.

Address for correspondence: Prof Makoto Naito, MD, Department of Cellular Function, Division of Cellular and Molecular Pathology, Niigata University Graduate School of Medical and Dental Sciences, Asahimachi-dori 1, Niigata 951-8510 Japan
Tel: +81-25-227-2102, Fax: +81-25-227-0761
E-mail: mnaito@med.niigata-u.ac.jp

Introduction

The physiological importance of heme oxygenase stems from its function as the initial and rate-limiting enzyme in heme degradation (Maines, 1988; Maines and Kappas, 1977). Bilirubin is derived mainly from the breakdown of hemoglobin and partly from various heme proteins. The oxidative degradation of these heme molecules is carried out by two distinct isozymes, HO-1 and HO-2 (Shibahara *et al.*, 1985; Maines, 1988; Cruse and Maines, 1988). HO-2, a constitutive form, is known to be abundant in the brain, testis, and liver of rodents and humans (Cruse and Maines, 1988), whereas HO-1, also known as heat shock protein-32 (hsp32), is expressed in macrophages in response to variety of stressors (Maines and Kappas, 1977; Ewing and Maines, 1991; Rizzardini *et al.*, 1993). There have been only a few studies on HO-1 expression in non-macrophagic cells. We have observed that hepatocytes in Kupffer cell-depleted livers displayed marked HO-1 expression after ischemia/reperfusion (Kobayashi *et al.*, 2002). Heme oxygenase is expressed not only in macrophages but also in renal tubules in nephrotoxic nephritis(Mosley *et al.*, 1998). However, little information is available on the expression of HO-1 in developing tissues during ontogeny.

Kupffer cells are tissue resident macrophages in the liver and act as a potent effector of immune responses and the metabolism. Our previous studies showed that HO-1 is expressed in Kupffer cells and plays a significant role in the bilirubin metabolism (Hirano *et al.*, 2001; Kobayashi *et al.*, 2002). Kupffer cells develop from primitive/fetal macrophages in the fetal liver (Naito *et al.*, 1990 a, b). It has been shown that the heme oxygenase level in the fetal liver was above the adult level (Lin *et al.*, 1989), and that the capacity of the liver for bilirubin production is greater in fetuses than adult animals (Maines and Kappas, 1975; Abraham *et al.*, 1988). However, the cellular elements

expressing HO-1 in the fetal liver have not been clarified. The present study was thus designed to reveal the cellular expression of HO-1 in the fetal liver. HO-1 expression in other fetal tissues was also examined.

Materials and Methods

Animals

Male Wistar rats (260–300 g) were obtained from Charles River Inc. Japan (Tokyo) and maintained under standard conditions at the Laboratory Animal Center of Niigata University School of Medicine. All animals were allowed free access to laboratory chow and tap water. Rats were mated overnight. The day when vaginal plug formation was detected was counted as day 1. Three rats on the same day of pregnancy were killed by ether anesthesia, and the uteri were removed.

In all experiments, data are expressed as the mean ± SD of three rats.

Antibodies

The mouse monoclonal antibodies (MoAbs) GTS-1 and GTS-2 were generated as described previously (Goda *et al.*, 1998). GTS-1 and GTS-2 recognize HO-1 and HO-2, respectively. The rat resident macrophage MoAb Ki-M2R (BMA Biomedicals, Augst, Switzerland) and rat and human macrophage scavenger receptor class A (MSR-A) MoAb SRA-E5 were used at a dilution of 1:100. SRA-E5 was generously supplied by Prof. M Takeya, Kumamoto University School of Medicine.

Immunohistochemistry

Fetal livers and other tissues from days 10 to 20 of gestation and neonatal tissues at birth, and 7, 14 and 56 days after birth were fixed for 4 h at 4℃ in periodate lysine-paraformaldehyde (PLP). The samples were sequentially washed for 4 h with PBS containing 10, 15, and 20% sucrose and were embedded in an OCT compound (Miles, Elkhart, IN). The sections (10 μm thick) were treated with avidin, biotin, and normal horse serum to minimize non-specific staining. They were incubated with monoclonal antibodies (MoAb) GTS-1 or GTS-2 dissolved in 1% BSA/PBS at a final concentration of 1 μg/ml for at least 2 h at 25℃ or overnight at 4℃. After several washes with PBS, the sections were stained with anti-mouse IgG for 1 h (Vectastain Elite ABC kit, Vector,CA). To prevent endogenous peroxidase reactions, the samples were pretreated with 0.3% H_2O_2 in cold methanol for 30 min (Isobe *et al.*, 1977) and were subsequently incubated with avidin and HRP-conjugated biotin for 30 min. Finally, 0.1 mg/ml of 3,3'-diaminobenzidine (DAB) tetrahydrochloride was applied to sections for 5 min. In order to assign the HO-associated immunostaining, the sections were counterstained with methyl green after fixation with formaldehyde for 20 min and the slides were coverslipped with an aqueous mounting medium. The immunohistochemical staining patterns were examined using samples collected from three individual rats. To confirm the specificity of the immuunohistochemical localization, antibodies preabsorbed with an excess of antigen were used. The numbers of HO-1-, Ki-M2R-, and SRA-E5-positive cells with nuclei per mm^2 were counted using a micrometer.

In separate sets of experiments, sections of the liver were double-stained to identify different types of nonparenchymal cells. To accomplish this, anti-rat macrophage MoAbs, Ki-M2R, HO-1, and SRA-E5 were used to stain Kupffer cells. In brief, the sections were immunostained using the first primary MoAbs and DAB as described above. After a wash with a glycine/HCl buffer for 1 h, the sections were incubated with the second primary MoAbs, biotin-conjugated anti-mouse IgG, and a complex of avidin and HRP-conjugated biotin under the same conditions as those for the primary MoAbs. Finally, DAB and nickel chloride were applied to the sections to stain single positive cells for second primary MoAbs purplish blue and double positive cells for both primary MoAbs dark brown, as described elsewhere (Yamamoto *et al.*, 1996).

Fig. 1. **a:** Yolk sac at 10 days of gestation. A few mononuclear cells (arrows) among hematopoietic cells and the endodermal layer (arrowheads) express HO-1. Immunohistochemical staining using GTS-1. ×1,000. **b:** HO-1-positive macrophages are scattered in the fetal liver at 13 days of gestation. Immunohistochemical staining using GTS-1. ×200. **c:** Fetal liver at 13 days of gestation. Macrophages express both HO-1 (brown) and MSR-A (black). Immunohistochemical double staining using GTS-1 and SRA-E5. ×1,000. **d:** HO-1 expression is observed in macrophages in the spleen at 20 days of gestation. Immunohistochemical staining using GTS-1. ×200. **e:** HO-1-expressing cells are observed in bone marrow at 20 days of gestation. Immunohistochemical staining using GTS-1. ×400. **f:** HO-1 expression is observed not only in macrophages (arrows) in the lamina propria but also in the mucosal epithelial cells (arrowheads) of the intestine in neonatal rats. Immunohistochemical staining using GTS-1. ×100

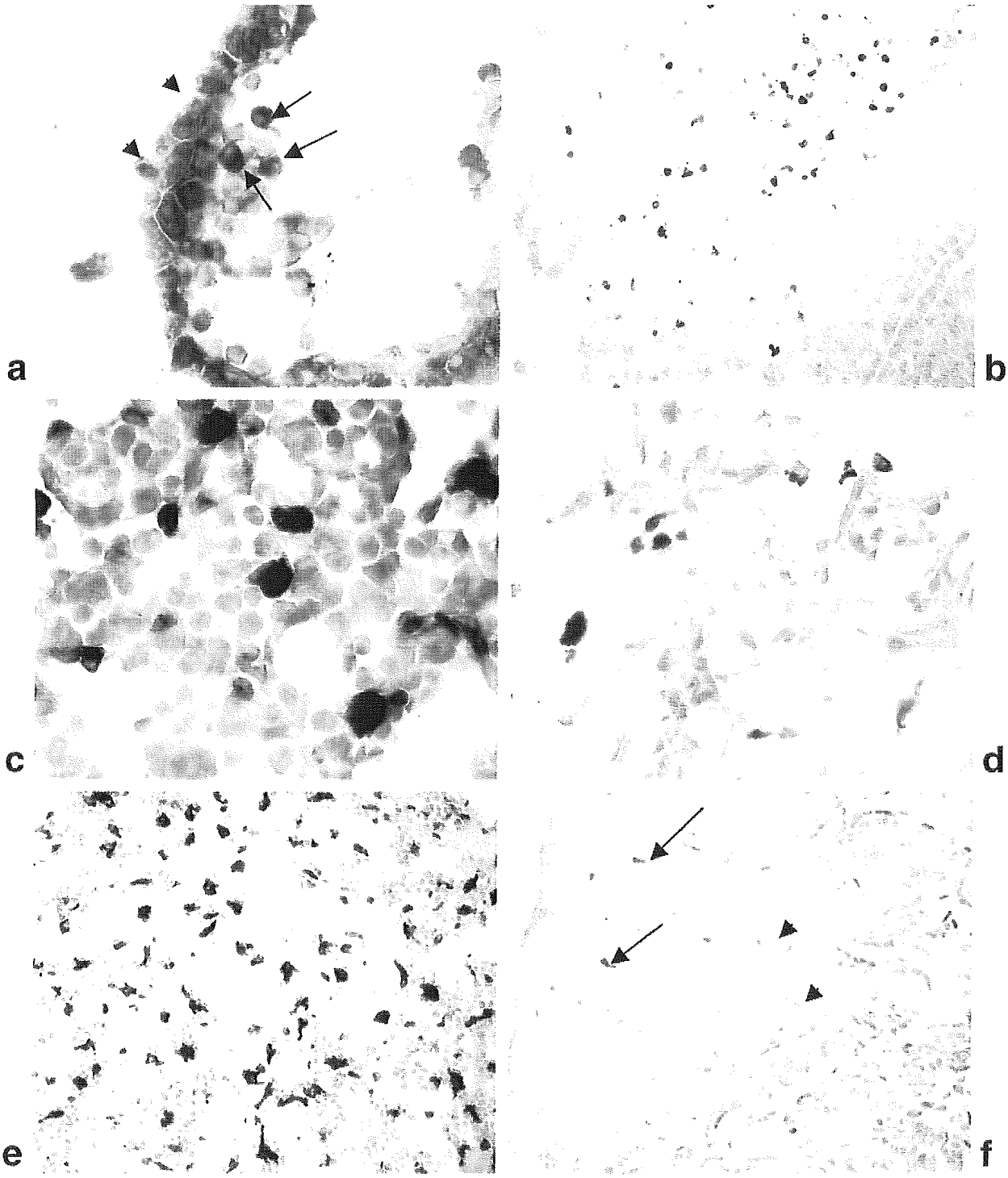

Fig. 1. Legend on the opposite page.

Isolation of RNA and analysis of messenger RNA (mRNA) by reverse transcrsption-polymerase chain reaction (RT-PCR)

Total cellular RNA was isolated by guanidinium thiocyanate-phenol-chloroform extraction from the liver (Yamamoto *et al.*, 1996). The total RNA (2 μg) was converted to cDNA by reverse transcription using a Super-Script Preamplification kit (Gibco BRL, Gaithersburg, MD) with the oligo (dT) primer. PCR amplification was performed with a Program Temp Control System PC-800 (ASTEC, Tokyo). Amplification was achieved using an initial cycle of 50℃ for 2 min and 95℃ for 10 min, followed by 26 cycles of 95℃ for 15 sec and 50℃ for 1 min. PCR was carried out with the following primers: HO-1 forward: 5'-TGGCTTTTTTCACCTTCCCG-3', reverse: 5'-TAAA TTCCCACTGCCACGGT-3', smooth muscle actin forward: 5'-TGGAATCCTGTGGCAT GCA TGA AC-3', reverse: TAAAACGCAGCTCAG TAACAGTCCG-3', and MSR-A forward: CCATGTCCTTGCAAGGTCTG, reverse: GTCTGAGGTCGTTGGTGATG. Primers were made to order by Takara (Tokyo).

Statistics

The significance of the data was evaluated by Student's *t*-test.

Results

Expression of HO-1 in macrophages

No HO-1-positive cells were detected in the fetal tissue at nine days of gestation except in the endodermal layer of the yolk sac. Immature hematopoietic cells were observed in the yolk sac at 10 days of gestation, and a few small round-shaped HO-1-positve cells were present in the vascular lumen of the yolk sac (Fig. 1a).

Hematopoiesis, mainly erythropoiesis, was observed in the fetal liver from 13 days of gestation. The HO-1 immunostaining was scattered in the fetal liver (Fig. 1b). Hepatic hematopoiesis was most prominent at 18 days of gestation. Erythrophagocytosis by HO-1-positive macrophages was remarkable. Immunohistochemical double staining demonstrated that HO-1- and SRA-E5-positive cells were almost identical cell populations (Fig. 1c). Bone marrow was formed from 18 days of gestation, and HO-1-positive cells were intermingled among a few hematopoietic cells (Fig. 1d).

A few small cells positive for HO-1 and SRA-E5 were distributed in the interstitium of the lung and neural tube in the early stage of fetal development. HO-1-positive cells in these tissues became larger and amoeboid with time. At 20 days of gestation, round or stellate-shaped cells expressing HO-1 were detected in the spleen (Fig. 1e), heart, intestine

Table 1. HO-1-expressing cells in the fetal and adult rat tissues

	Fetus					Newborn						Adult
Days	10	13	15	18	20	0	1	3	5	7	14	56
Macrophages												
Liver	−	+	++	+++	++	+	+	+	+	+	+	+
Spleen	ND	ND	ND	ND	+	++	+++	+++	+++	+++	+++	+++
Bone marrow	−	−	−	±	±	+	+	+	+	+	+	+
Yolk sac	+	+	+	+	+							
Lung	−	−	±	±	+	++	++	+	±	±	±	±
Heart	−	−	−	−	−	±	±	±	±	±	±	±
Intestine	−	−	−	−	±	+	+	+	+	+	+	+
Mesenchyme	−	±	±	±	±	±						
Neural tube	−	±	±	±	±							
Kidney	ND	ND	ND	±	±	+	+	+	±	±	±	±
Non-macrophages												
Chorionic villi	+	+	+	+	+							
Renal tubules	ND	ND	ND	+	+	++	++	+	+	+	+	+

ND: not detected, −: negative, ±: <10/high power field (HF), +: >10/HF, ++: >20/HF, +++: >30/HF

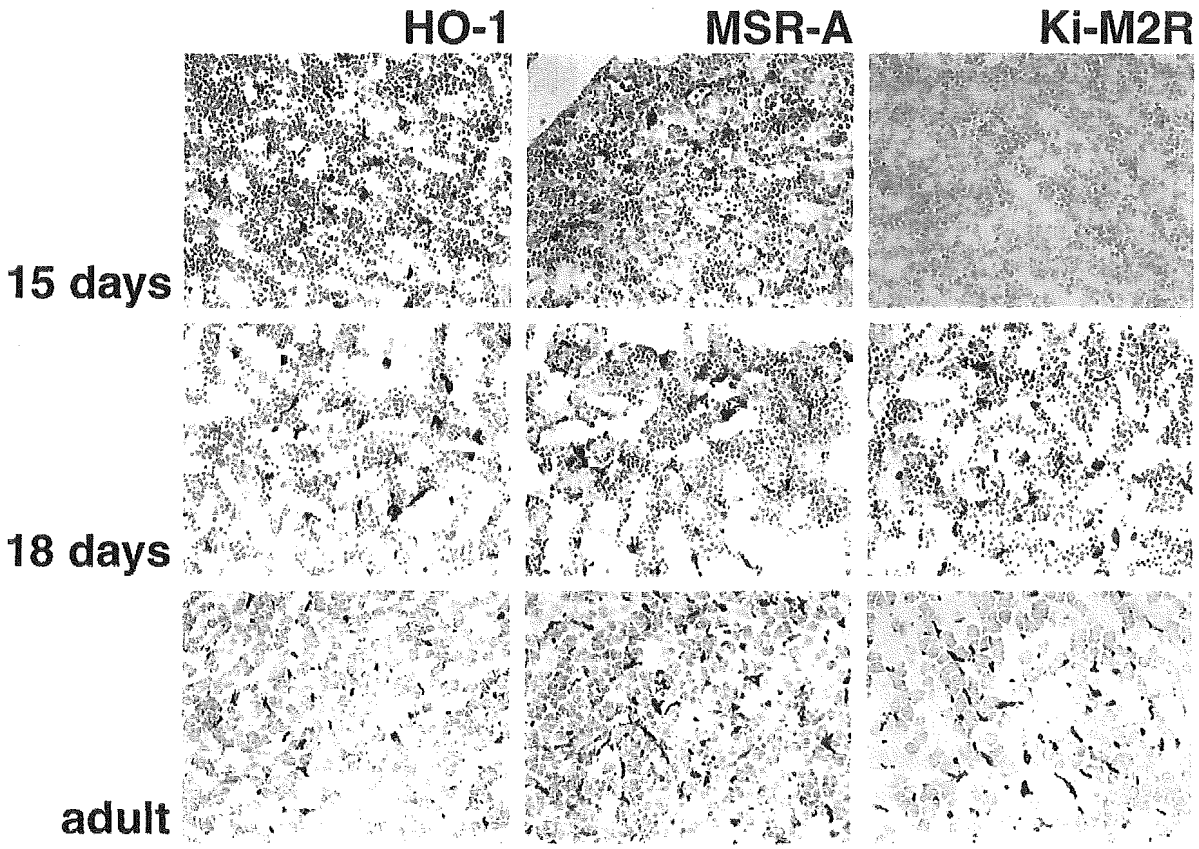

Fig. 2. HO-1, scavenger receptor, and resident macrophage marker (Ki-M2R) expression in the fetal (15 and 18 days of gestation) and adult liver. HO-1- and MSR-A-positive cell numbers increase with the time during the fetal period, but decrease after birth. In contrast, Ki-M2R-positive cells are absent at 15 days and appear at 18 days of gestation. Immunohistochemical staining using GTS-1, SRA-E5, and Ki-M2R. ×100

(Fig. 1f), and kidney (Table 1). HO-1 positive cells were observed in the mesenchymal tissue of the fetus throughout the gestational period (Table 1).

We then compared the expression of HO-1, MSR-A and Ki-M2R in the liver. The density in HO-1- and MSR-A-positive cells became more predominant with time (Fig. 2). The HO-1 and MSR-A positively stained cells were polygonal and round at 13 days of gestation and slender or irregular in shape after 18 days of gestation. Cells expressing HO-1 and MSR-A gradually decreased in number in the liver after birth (Fig. 3). In contrast, Ki-M2R-positive cells were not observed until day 18 of gestation, and the numbers of Ki-M2R- and SRA-E5-positive cells were similar after birth. HO-1 immunoreactivity was not found in hepatocytes throughout the gestational period.

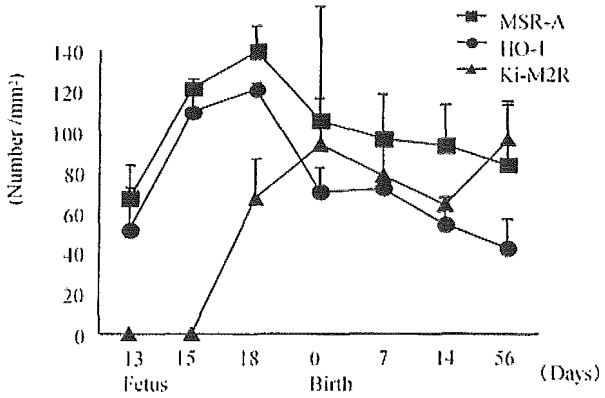

Fig. 3. Numbers of HO-1, MSR-A and Ki-M2R-expressing cells in the fetal and neonatal liver.

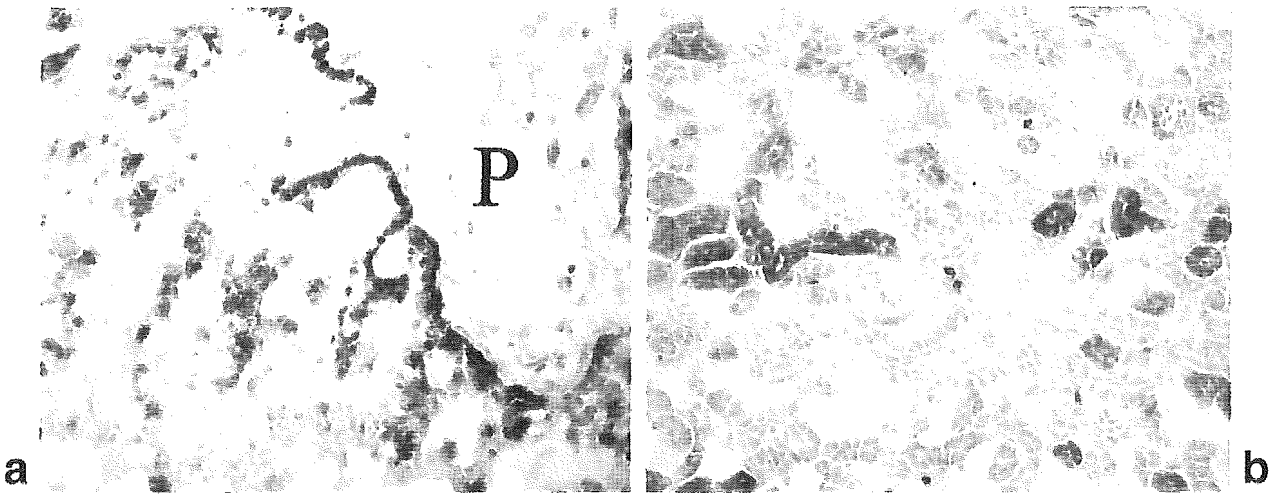

Fig. 4. HO-1 expression in the placenta and kidney. **a:** HO-1 expression is observed in the syncytiotrophoblasts and cytotrophoblasts of the chorionic villi. P: placenta. *Immunohistochemical staining using GTS-1.* ×200. **b:** *HO-1 expression* is observed in the renal proximal and distal tubules at 18 days of gestation. Immunohistochemical staining using GTS-1. ×200

Expression of HO-1 in non macrophagic cells

HO-1 proteins were immunolocalized in the endodermal layer of the yolk sac and syncytiotrophoblasts and the underlying cytotrophoblasts throughout the fetal period (Fig. 4a). At 18 days of gestation, HO-1 immunoreactivity was observed in the renal proximal and distal tubules (Fig. 4b). HO-1 expression was also observed in mucosal epithelial cells in intestines after birth (Fig. 1f). These HO-1-expressing cells were judged as non-macrophagic cells.

Expression of HO-1 mRNA in fetal liver

The expression of HO-1 and MSR-A mRNA peaked at 18 days of gestation (Fig. 5). HO-1 and MSR-A mRNA levels paralleled the intensity of HO-1 and MSR-A immunoreactivity. The expression of HO-2 in the livers of both groups of rats was unchanged (data not shown).

Discussion

We have reported that small and immature macrophages first appear in the yolk sac and termed these cells primitive macrophages (Takahashi *et al.*, 1989; Naito *et al.*, 1990a,b; Takahashi and Naito, 1993). Primitive macrophages are characterized by their small round shape, the expression of macrophage antigens, and phagocytic capacity. Primitive macrophages differentiate into larger and amoeboid-shaped fetal macrophages. In the present study, we observed that HO-1-positive cells comparable to primitive/fetal macrophages appeared in the yolk sac and fetal liver. Immunohistochemical double staining demonstrated that HO-1-positive cells also expressed MSR-A. Because MSR-A is a macrophage-specific receptor (Naito *et al.*, 1992), HO-1 is a marker of primitive/fetal macrophages.

It was demonstrated that the HO-1 mRNA level in the fetal liver was above the adult level and reached a maximum 24 h after birth (Lin *et al.*, 1989). It is also reported that the capacity of the liver for bilirubin production is greater in fetuses than in adults (Maines and Kappas, 1975; Abraham *et al.*, 1988). However, there has been no immunohistochemical observation of HO-1 expression in the fetal liver. This study confirmed that HO-1 is expressed in a large number of macrophages in the liver. The fetal liver is a hematopoietic organ, and macrophages scavenge a large number of erythroid cells. During hepatic hematopoiesis, macrophages in the fetal liver actively phagocytize erythroid cells. Hepatic hematopoiesis was most active at 18 days of gestation and the density of HO-1-expressing cells was greatest at 18 days of gestation, while only half of the Kupffer cells expressed HO-1 at 14 days after birth. We have reported that in adult rats, about 30% of Kupffer cells expressed HO-1, and this HO-1 expression was enhanced after phagocytosis of heat-denatured erythrocytes (Hirano *et al.* 2001). These findings indicate that active hemophagocytosis is closely related to the enhanced expression of HO-1 in macrophages in the fetal liver.

In contrast to HO-1 and scavenger receptors expressed in

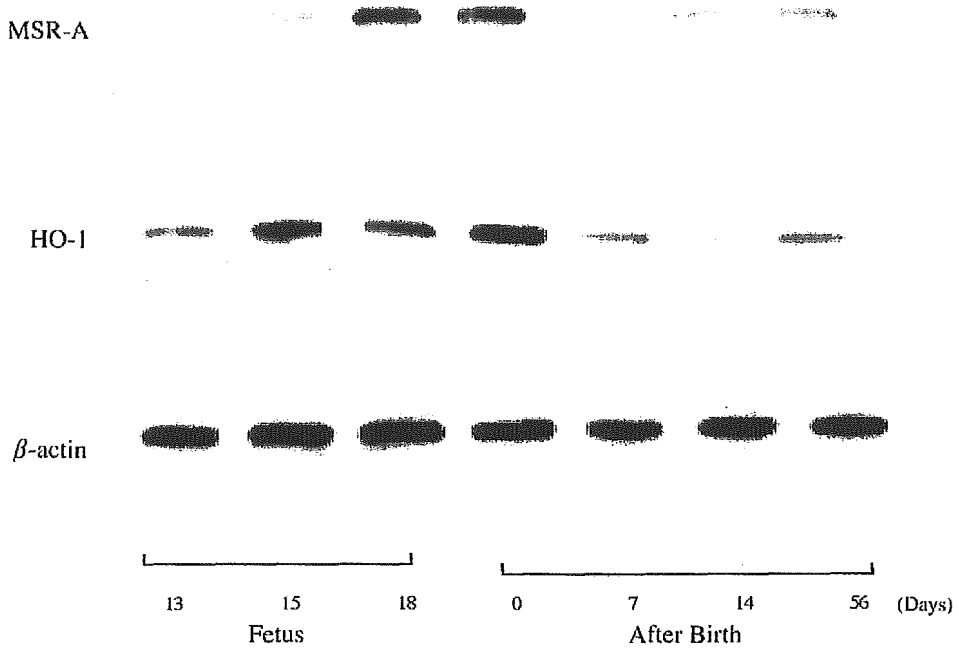

Fig. 5. Expression of HO-1 and MSR-A mRNAs in fetal and neonatal rat livers (RT-PCR).

macrophages early in the fetal period, Ki-M2R reacted with macrophages after 18 days of gestation. Peroxidase activity, which is an enzymatic marker for resident macrophages, also develops after 18 days of gestation in the fetal rat (Naito and Wisse, 1977). The expression of Ki-M2R and peroxidase activity have been confirmed in all of the Kupffer cells. Based on these findings, Ki-M2R can be said to recognize resident macrophages in both fetal and adult tissues.

Besides macrophages. HO-1 was expressed in chorionic villi of the placenta, endodermal layer of the yolk sac, renal tubular cells, and other tissues. HO-1 immunolocalization was localized in the syncytiotropholast layer of the chorionic villi, and both HO-1 and HO-2 protein expression was decreased in damaged chorionic villi (Lash *et al.*, 2002). The previous and present results both suggest that HO-1 plays an important role not only in heme catabolism but also in the maintenance of pregnancy.

HO-1 expression was also confirmed in the renal tubules. The first human case of heme oxygenase-1 (HO-1) deficiency was characterized by hemolytic anemia and intravascular hemolysis with a low bilirubin level (Yachie *et al.*,1999). Electron microscopy of renal glomeruli of the patient revealed detachment of the endothelium, suggesting vulnerability to stressful injury to kidney. Ohta *et al.* (2000) examined HO-1 expression in the kidneys of patients with various diseases and found HO-1 expression in renal tubules in both healthy and diseased kidneys and in macrophages in the glomeruli of some nephropathies. A similar result was reported in rats (Mosley *et al.*, 1998). It was further demonstrated that the induction of HO-1 expression had protective effects on nephrotoxic nephritis in Lewis rats. These results suggest that HO-1 is important for protecting renal tubules from oxidative stress.

The significance of the HO-1 expression in the endodermal layer of the yolk sac and intestinal mucosal epithelial cells remains unknown. Because HO-1 expression was first confirmed in mucosal epithelial cells after birth, maternal milk may have induced the expression in the neonatal rat intestine. The expression of HO-1 in some developing tissues implies that HO-1 bears pleiotropic roles in these tissues.

Acknowledgments

We thank Mr. K Sato, S Momozaki, K Ohyachi, Miss K Miyamoto, Y Aizawa, and Ms. K Moriki for their excellent technical assistance.

References

Abraham NG, Lin JH, Mitrione SM, Schwartzman ML, Levere RD, Shibahara S: Expression of heme oxygenase gene in rat and human liver. *Biochem Biophys Res Commun* 150: 717-22 (1988).

Cruse I, Maines MD: Evidence suggesting that the two forms of heme oxygenase are products of different genes. *J Biol Chem* 263: 3348-3353 (1988).

Ewing JF, Maines MD: Rapid induction of heme oxygenase 1 mRNA and protein by hyperthermia in rat brain: heme oxygenase 2 is not a heat shock protein. *Proc Natl Acad Sci USA* 88: 5364-5368 (1991).

Goda N, Suzuki K, Naito M, Takaoka S, Tsuchida E, Ishimura Y, Tamatani T, Suematsu M: Distribution of heme oxygenase isoforms in rat liver. Topographic basis for carbon monoxide-mediated microvascular relaxation. *J Clin Invest* 101: 604-612 (1998).

Hirano K-I, Kobayashi T, Watanabe T, Yamamoto T, Hasegawa G, Hatakeyama K, Suematsu M, Naito M: Role of heme oxygenase-1 and Kupffer cells in the production of bilirubin in the rat liver. *Arch Histol Cytol* 64: 111-120 (2001).

Isobe Y, Chen ST, Nakane PK, Brown WR: Studies on translocation of immunoglobulins across intestinal epithelium. I. Improvements in the peroxidase-labeled antibody method for application to study of human intestinal mucosa. *Acta Histochem Cytochem* 10: 161-171 (1977).

Kobayashi T, Hirano K, Yamamoto T, Hasegawa G, Hatakeyama K, Suematsu M, Naito M: Protective role of Kupffer cells in ischemia-reperfused rat liver. *Arch Histol Cytol* 65: 251-261 (2002).

Lash GE, McLaughlin BE, Macdonald-Goodfellow SK, Smith GN, Brien JF, Marks GS, Nakatsu K, Graham CH: Relationship between tissue damage and heme oxygenase expression in chorionic villi of term human placenta. *Am J Physiol Heart Circ Physiol* 284: H160-167 (2002).

Lin JHC, Villalon P, Nelson JC, Abraham NG: Expression of rat liver heme oxygenase gene during development. *Arch Biochem Biophys* 270: 623-629 (1989).

Maines MD: Heme oxygenase: function, multiplicity, regulatory mechanisms, and clinical applications. *FASEB J* 2: 2557-2568 (1988).

Maines MD, Kappas A: Study of the developmental pattern of heme catabolism in liver and the effects of cobalt on cytochrome P-450 and the rate of heme oxidation during the neonatal period. *J Exp Med* 141: 1400-1410 (1975).

Maines MD, Kappas A: Metals as regulators of heme metabolism: physiological and toxicological implications. *Science* 198: 1215-1221 (1977).

Mosley K, Wembride DE, Cattell V, Cook HT: Heme oxygenase is induced in nephrotoxic nephritis and hemin, a stimulator of heme oxygenase synthesis, ameliorates disease. *Kidney Int* 53: 672-678 (1998).

Naito M, Wisse E: Observations on the fine structure and cytochemistry of sinusoidal cells in fetal and neonatal rat liver. In: *Kupffer cells and other liver sinusoidal cells* (Wisse E, Knook DL, ed). Elsevier/North-Holland Biomedical Press, Amsterdam, 1977 (p.497-505).

Naito M, Takahashi K, Nishikawa S-I: Development, differentiation and maturation of macrophages in the fetal mouse liver. *J Leukoc Biol* 48: 27-37 (1990a).

Naito M, Yamamura F, Nishikawa S-I, Takahashi K: Development, differentiation, and maturation of fetal mouse yolk sac macrophages in cultures. *J Leukoc Biol* 46: 1-10 (1990b).

Naito M, Suzuki H, Mori T, Kodama T, Matsumoto A, Takahashi K: Coexpression of type I and II human macrophage scavenger receptors in macrophages in various organs and foam cells in atherosclerotic lesions. *Am J Pathol* 141: 591-599 (1992).

Ohta K, Yachie A, Fujimoto K, Kaneda H, Wada T, Toma T, Seno A, Kasahara Y, Yokoyama H, Seki H, Koizumi S: Tubular injury as a cardinal pathologic feature in human heme oxygenase-1 deficiency. *Am J Kidney Dis* 35: 863-70 (2000).

Rizzardini M, Terao M, Falcini F, Cantoni L: Cytokine induction of haem oxygenase mRNA in mouse liver. *Biochem J* 290: 343-347 (1993).

Shibahara S, Muller R, Taguchi H, Yoshida T: Cloning and expression of cDNA of rat heme oxygenase. *Proc Natl Acad Sci USA* 82: 7865-7869 (1985).

Takahashi K, Naito M: Development, differentiation, and proliferation of macrophages in the rat yolk sac. *Tissue Cell* 25: 351-362 (1993).

Takahashi K, Yamamura F, Naito M: Differentiation, maturation, and proliferation of macrophages in the mouse yolk sac: A light-microscopic, enzyme-cytochemical, immunohistochemical, and ultrastructural study. *J Leukoc Biol* 45: 87-96 (1989).

Yachie A, Niida Y, Wada T, Igarashi N, Kaneda H, Toma T, Ohta K, Kasahara Y, Koizumi S: Oxidative stress causes enhanced endothelial cell injury in human heme oxygenase-1 deficiency. *J Clin Invest* 103: 129-135 (1999).

Yamamoto T, Naito M, Moriyama H, Umezu H, Matsuo H, Kiwada H, Arakawa M: Repopulation of murine Kupffer cells after intravenous administration of liposome-encapsulated dichrolomethylene diphosphonate. *Am J Pathol* 149: 1271-1286 (1996).

Infrared Spectroscopic and Mutational Studies on Putidaredoxin-Induced Conformational Changes in Ferrous CO-P450cam[†,‡]

Shingo Nagano,[*,#,$] Hideo Shimada,[*,#] Akiko Tarumi,[#] Takako Hishiki,[#] Yoko Kimata-Ariga,[#,⊥] Tsuyoshi Egawa,[#,∥] Makoto Suematsu,[#] Sam-Yong Park,[§,+] Shin-ichi Adachi,[§] Yoshitsugu Shiro,[§] and Yuzuru Ishimura[#,&]

Department of Biochemistry and Integrative Medical Biology, School of Medicine, Keio University, 35 Shinano-machi, Shinjuku-ku, Tokyo 160-8582, Japan, and The Institute of Physical and Chemical Research (RIKEN), RIKEN Harima Institute, 1-1-1 Kouto, Mikazuki-cho, Sayo, Hyogo 679-5148, Japan

Received August 6, 2003; Revised Manuscript Received October 6, 2003

ABSTRACT: Ferrous-carbon monoxide bound form of cytochrome P450cam (CO-P450cam) has two infrared (IR) CO stretching bands at 1940 and 1932 cm^{-1}. The former band is dominant (>95% in area) for CO-P450cam free of putidaredoxin (Pdx), while the latter band is dominant (>95% in area) in the complex of CO-P450cam with reduced Pdx. The binding of Pdx to CO-P450cam thus evokes a conformational change in the heme active site. To study the mechanism involved in the conformational change, surface amino acid residues Arg79, Arg109, and Arg112 in P450cam were replaced with Lys, Gln, and Met. IR spectroscopic and kinetic analyses of the mutants revealed that an enzyme that has a larger 1932 cm^{-1} band area upon Pdx-binding has a larger catalytic activity. Examination of the crystal structures of R109K and R112K suggested that the interaction between the guanidium group of Arg112 and Pdx is important for the conformational change. The mutations did not change a coupling ratio between the hydroxylation product and oxygen consumed. We interpret these findings to mean that the interaction of P450cam with Pdx through Arg112 enhances electron donation from the proximal ligand (Cys357) to the O−O bond of iron-bound O_2 and, possibly, promotes electron transfer from reduced Pdx to oxyP450cam, thereby facilitating the O−O bond splitting.

Cytochrome P450cam (P450cam)[1] is a heme-containing monooxygenase that catalyzes the hydroxylation of D-camphor in *Pseudomonas putida* (*1*, *2*). The ferric D-camphor-free enzyme first binds D-camphor to give the ferric D-camphor-bound state. This substrate-bound form then accepts one electron from reduced putidaredoxin (Pdx), yielding a substrate-bound ferrous form. Subsequent binding of O_2 to the ferrous form produces a D-camphor-bound ferrous-O_2 derivative (oxyP450cam). Upon a second one-electron reduction by Pdx, the oxyP450cam derivative proceeds to the D-camphor hydroxylation reaction, yielding 5-*exo*-hydroxycamphor and water and regenerating the ferric substrate-free resting state. Two protons are required for this reaction and are delivered into the active site of the enzyme through a proton delivery system (*3*−*7*).

Two redox-linked proteins, a flavoprotein putidaredoxin reductase (PdR) and an iron−sulfur protein Pdx, are necessary for transfer of two electrons from NADH to P450cam (*1*, *2*). On the other hand, other iron−sulfur proteins such as spinach ferredoxin and beef adrenodoxin readily provide the first electron but not the second one to support the D-camphor hydroxylation (*8*). On the basis of these and other findings, Lipscomb et al. proposed that, in addition to be an electron shuttle, Pdx plays a role as an "effector" in the D-camphor monooxygenation reaction. Since then, various spectroscopic studies including NMR (*9*−*11*), EPR (*12*), IR (*13*), and resonance Raman (*14*, *15*) have been carried out to examine the interaction between P450cam and Pdx. The

[†] This work was supported in part by grants-in-aid for scientific research on priority areas, scientific research (C), and the 21st Century Center of Excellence (COE) Program Entitled "Understanding and Control of Life's Function via Systems Biology (Keio University)" from Ministry of Education, Science, Culture, Sports and Technology of Japan and by grants from Keio University.

[‡] The structural coordinates and the structure factors are deposited in the Protein Data Bank under accession codes 1IWI, 1IWJ, and 1IWK for ferric D-camphor bound forms of wild-type P450cam, R109K, and R112K mutants, respectively.

* To whom correspondence should be addressed. E-mail: shimada@sc.itc.keio.ac.jp; fax: 81−3−3358−8138; phone: 81−3−3353−1997. E-mail: snagano@uci.edu; fax: 1−949−824−3280; phone: 1−949−824−4322

[#] Keio University.

[§] RIKEN Harima Institute.

[$] Present address: Department of Molecular Biology and Biochemistry and the Program in Macromolecular Structure, University of California, Irvine, Irvine CA 92697-3900 USA.

[⊥] Present address: Division of Enzymology, Institute for Protein Research, Osaka University, Yamadaoka 3−2, Suita, Osaka 565-0871, Japan.

[+] Present address: Protein Design Laboratory, Graduate School of Integrated Science, Yokohama City University, 1−7−29 Suehiro-cho, Tsurumi, Yokohama 230-0045, Japan.

[&] Present address: Department of Biochemistry, The University of Texas Health Science Center at San Antonio, San Antonio, TX 78229-3900, USA.

[∥] Present address: Department of Biochemistry and Biophysics, University of Pennsylvania.

[1] Abbreviations: P450cam, cytochrome P450 (CYP101) originally isolated from *Pseudomonas putida*. It catalyzes the conversion of D-camphor to 5-*exo*-hydroxycamphor; PdR, putidaredoxin reductase; Pdx, putidaredoxin; oxyP450cam, D-camphor-bound ferrous-O_2 P450cam; CO-P450cam, D-camphor-bound ferrous-carbon monoxide P450cam, IR; infrared, EPR; electron paramagnetic resonance.

10.1021/bi035410p CCC: $25.00
Published on Web 11/19/2003

Table 1: Kinetic and Spectroscopic Properties of Wild-Type P450cam and Its Mutants

protein	O_2 consumption rate (μM min^{-1} (μM enzyme)$^{-1}$)	coupling ratio[a] (%)	k_2[b] (s^{-1})	band II intensity[c] (arbitrary unit)	K_d^{IR} (μM)[d]	K_d^{kin} (μM)[e]
WT	1400 (100%)	100	169	0.97 ± 0.09	22	12
R109K	500 (36%)	100	126	0.18 ± 0.06	79	47
R109Q	100 (7%)	100	66	0.09 ± 0.09	916	208
R112K	200 (14%)	88	87	0.16 ± 0.02	38	76
R79Q	1480 (106%)	100	N.D.[f]	*g*	N.D.[f]	N.D.[f]
R112M	1.7 (0.1%)[h]	86[h]	*i*	*j*	N.D.[f]	N.D.[f]

[a] Ratio between the hydroxylated product (5-*exo*-hydroxy camphor) and O_2 consumed. [b] Apparent rate constants for breakdown of oxyP450cam/Pdx complex. [c] Band II area of CO-P450cam/Pdx complex relative to the whole band area. Data are mean ± standard deviation. [d] Apparent dissociation constants calculated from IR titration. [e] Apparent dissociation constants calculated from kinetic analysis of breakdown of oxyP450cam/Pdx complex. [f] Not determined. [g] Addition of 5-fold excess amount of reduced Pdx gives almost identical spectrum of wild-type CO-P450cam/Pdx complex. [h] Data from Unno et al. (*20*). [i] OxyR112M in the presence of 200-fold excess of reduced Pdx does not decay over 500 ms. [j] No significant ν_{CO} spectral change was observed even when 20-fold excess of reduced Pdx was added.

results have established unambiguously that Pdx binding produces significant changes in the structure of the heme active center in P450cam. However, the molecular mechanism by which the conformational change occurs and the significance of the conformational change remain unclear.

In the present study, we examined effects of mutation at the presumed Pdx-binding site of P450cam on the conformational change as well as the catalytic properties of P450cam; Arg79, Arg109, Arg112 are the residues in the presumed Pdx binding site (*16*). Among them, Arg109 and Arg112 mutants showed significantly decreased catalytic activities together with decreased binding affinities to Pdx. X-ray crystallographic and IR spectroscopic studies indicated that the overall structures of 109 and 112 mutants are not eminently different from that of the wild-type P450cam. However, both mutants exhibited much less conformational conversion than that occurring in the wild-type P450cam upon complex formation with Pdx, presumably due to the lack of hydrogen bonding between Arg112 and Pdx. On the basis of these results, the molecular mechanism and functional significance of the conformational change are discussed.

EXPERIMENTAL PROCEDURES

Enzyme Purification and Assay. The mutagenesis of the P450cam gene was performed as previously described (*5*, *17*). The wild-type P450cam and its mutants were expressed in *Escherichia coli* strain JM109 and purified according to the procedures described previously (*18*). Purified P450cam with an *RZ* value (A_{391}/A_{280}) greater than 1.5 was used in this study unless otherwise stated. Pdx and PdR were also expressed in *Escherichia coli* strain JM109 and were purified to a homogeneous state according to the methods described by Gunsalus and Wagner (*19*). Catalytic activity of P450cam was determined by measuring simultaneously oxygen consumption and NADH oxidation at 20 °C in a reconstituted system composed of 360 μM NADH, 14 μM Pdx, 0.12 μM PdR, and an appropriate amount of P450cam in 50 mM potassium phosphate, pH7.4, containing 50 mM KCl and 1 mM D-camphor (hereafter designated buffer A) (*5*, *18*). The activity of the wild-type P450cam and its mutants, R79Q, R109K, R109Q, and R112K was measured in this work and presented in Table 1, while that of R112M was presented elsewhere (*20*).

The rates for degradation of oxyP450cam into ferric enzyme and 5-*exo*-hydroxycamphor upon reaction with reduced Pdx were measured at 4 °C by monitoring the spectral changes of oxyP450cam from 380 to 540 nm on a Unisoku stopped-flow/rapid-scan spectrophotometer, model RSP-601 (Osaka, Japan) as described previously (*5*). The reaction between oxyP450cam and reduced Pdx is shown as follows:

$$A + B \rightleftarrows C \xrightarrow{k_2} D$$

In this reaction scheme, species A and B represent oxyP450cam and reduced Pdx, respectively. Species C shows the oxyP450cam/Pdx complex and D represents the product proteins, ferric P450cam and oxidized Pdx. The bimolecular association is, as shown in the previous study (*21*), sufficiently faster than the breakdown of the oxyP450cam/Pdx complex. An excess amount of Pdx over P450cam was used for this experiment. In such a case, the observed rate constants (k_{obs}) are expressed as eq i (*22*)

$$k_{obs} = k_2[\mathrm{Pdx}]/(K_d^{kin} + [\mathrm{Pdx}]) \quad \text{(i)}$$

where k_2 is the apparent rate constant for the breakdown of the oxyP450cam/Pdx complex, K_d^{kin} is the apparent dissociation constant for the oxyP450cam/Pdx complex, and [Pdx] is the initial concentration of reduced Pdx, which is sufficiently larger than the P450cam concentration.

Measurement of IR ν_{C-O} Spectra. CO-P450cam was prepared as follows: 80−100 μL of P450cam or a mixture of P450cam and Pdx in buffer A in a 3-mL vial sealed with a vaccine cap was made anaerobic by passing N_2 gas into the vial through the vaccine cap. Then sodium dithionite in alkaline buffer was added to reduce the protein. After reduction of the sample, the atmosphere of the vial was changed to CO using the procedure described above. The protein was anaerobically transferred to an IR cell (Specac, England) with 0.05-mm path length CaF_2 windows. IR spectra were measured at 20 °C with a PerkinElmer FT-IR spectrophotometer, system 2000 (Buckinghamshire, England) with an Hg/Cd/Te detector. A 1000 scan interferogram was collected in a single beam mode with 2 cm^{-1} resolution. Buffer A spectra obtained under identical conditions were used as reference spectra. UV−visible absorption spectra were measured before and after IR spectral measurements and no difference was found. A baseline of the spectra was corrected with a cubic spline function.

Analysis of IR Spectra. IR ν_{C-O} spectra of CO-P450cam were decomposed into single bands of Gaussian shape (*23*,

Table 2: Data Collection and Structure Refinement Statistics and Crystal Parameters

data set	wild type	R109K	R112K
resolution range (Å)	15.0−2.0	15.0−2.0	20.0−2.0
unit cell dimensions (Å)	a = 109.12 b =104.33 c = 36.18	a = 109.16 b = 104.33 c = 36.14	a = 104.18 b = 104.13 c = 36.65
reflections measured/unique	163,126/27,250	118,057/27,413	158,280/25,273
completeness overall/outer shell (2.11−2.00)	95.1/79.8	95.1/79.8	88.4/67.4
R_{merge} (%)[a] overall/outer shell (2.11−2.00)	3.2/6.1	3.3/5.4	9.0/41.3
redundancy	3.9	3.2	4.3
Refinement Statistics			
resolution range (Å)	15.0−2.0	15.0−2.0	20.0−2.0
σ cutoff	0.0	0.0	0.0
reflections used	27,215	27,370	24,998
R factor (%)[b]	17.3	16.6	17.9
R_{free} factor (%)[b]	22.9	22.1	23.2
no. of water molecules	187	180	175
RMS deviations from ideal			
bond length (Å)	0.007	0.007	0.006
bond angles (degree)	1.134	1.129	1.126
Ramachandran plot			
residues in most favorable regions (%)	91.1	91.1	90.8
residues in favorable regions (%)	8.9	8.9	9.2
residues in disallowed regions (%)	0.0	0.0	0.0

[a] $R_{merge} = \Sigma |I_i - <I>|/\Sigma|I_i|$, where I_i is the intensity of an observation and $<I>$ is the mean value for that reflection and the summations are overall reflections. [b] R factor $= \Sigma_h||F_o(h)| - |F_c(h)||/\Sigma_h|F_o(h)|$, where F_o and F_c are the observed and calculated structure factor amplitudes, respectively. R_{free} factor was calculated with 5% of the data.

24) with a minimal number of bands to obtain flat residuals (the differences between the observed and sums of componental bands). The decomposition was performed by using a multipeak fitting function of IgorPro software (WaveMetrics, Inc., Lake Oswego, OR). When Pdx-binding induced spectral changes were analyzed, the area of each componental band at the end point of titration and dissociation constants (K_d^{IR}) were determined by fitting the data using a least-squares minimization procedure of an equation corresponding to reversible binding of a 1:1 complex.

$$\Delta S = \Delta S_\infty\{L + K_d^{IR} + E - [(L + K_d^{IR} + E)^2 - 4EL]\}^{1/2}/2E \quad \text{(ii)}$$

In this equation, ΔS is the change in componental band area for a total Pdx concentration L. ΔS_∞ is the maximum change of componental band area, and E is the total P450cam concentration.

Crystallization and X-ray Crystallography. R109K and R112K mutants of P450cam were crystallized according to previously published procedures (*5*, *25*) and the X-ray crystallographic analysis was performed as described previously (*5*). P450cam samples with an *RZ* higher than 1.6 were employed for the crystallization. The data collection and refinement statistics and crystal parameters are given in Table 2.

RESULTS

Catalytic Activities. The catalytic activities of the wild-type enzyme and all mutant enzymes were measured as described under Experimental Procedures. The oxygen consumption rates and coupling ratios of oxygen consumption to the D-camphor monooxygenation (5-*exo*-hydroxycamphor/O_2 consumed in %) are listed in Table 1. The mutations of Arg109 and Arg112 at the presumed Pdx-binding site reduce the O_2 consumption rate to less than 40% of the wild-type enzyme. The values for R112K mutant were in good agreement with the previously reported values (*20*). The mutation at Arg79 had no effect on the enzymatic activities to wild type, suggesting that this residue is not important for activity. Although all the 109 and 112 mutants of P450cam investigated herein exhibit reduced oxygen consumption activities, they all catalyze the monooxygenation of D-camphor with a good coupling ratio (86−100%), indicating that oxyP450cam decomposes stoichiometrically into ferric P450cam, H_2O, and 5-*exo*-hydroxycamphor. This phenomenon is in contrast with the case of the Ala mutation at Thr252, which reduces the coupling ratio to 6% (*18*).

Reaction of oxyP450cam with Reduced Pdx. We next measured rates of decomposition of oxyP450cam with reduced Pdx for wild-type and mutant enzymes. Figure 1A,B shows time courses of the reactions of reduced Pdx with wild type and R112K, respectively. As shown, the experimental data fitted well to a single-exponential curve as reported previously for the wild-type enzyme (*20*). Time courses of the reaction catalyzed by wild-type P450cam as well as by its mutants always followed the first-order kinetics under different Pdx concentrations. Figure 2 shows plots of apparent first-order rate constant (k_{obs}) as a function of Pdx concentration. Rate constants (k_2) for breakdown of the

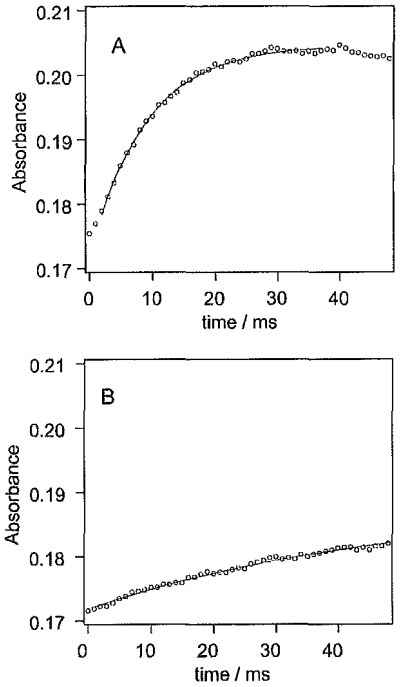

FIGURE 1: Stopped-flow analysis of the reaction between oxyP450cam and reduced Pdx. The reaction was followed by monitoring the changes in absorbance at 420 nm of P450cam after mixing oxyP450cam with reduced Pdx. Panel A represents the data for wild type, and panel B represents the data for R109K. The final concentrations of the reaction components after mixing were as follows: [P450cam] = 1.0 μM, [Pdx] = 10 μM, [metyrapone] = 5 mM. The reaction was performed at 4 °C in 50 mM K phosphate buffer, pH 7.4, containing 50 mM KCl and 1 mM D-camphor. The solid line through the experimental data points represents a single exponential fit to the data. OxyP450cam and reduced Pdx were prepared as described previously (*5*).

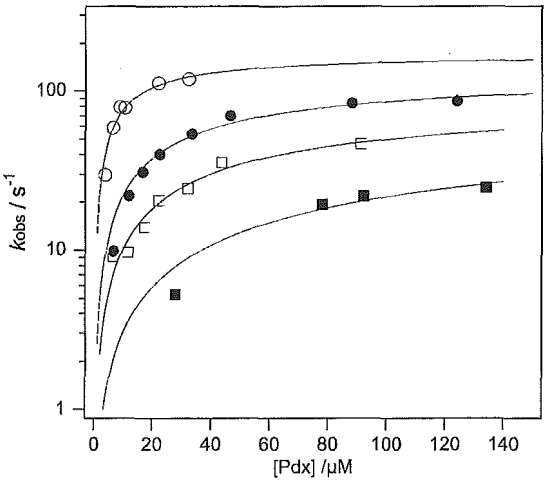

FIGURE 2: Observed rate constant (k_{obs}) for the reaction of oxyP450cam in the presence of a varying concentration of reduced Pdx. Rate constants were obtained from a single-exponential fitting to the time course data of the reaction such as those shown in Figure 1. k_{obs} values are shown for wild type (open circle), R109K (closed circle), R112K (open square), R109Q (closed square). The reaction was performed at 4 °C in 50 mM K phosphate, pH 7.4, containing 50 mM KCl and 1 mM D-camphor. Initial oxyP450cam concentration was fixed at 1.0 μM.

complex formed between oxyP450cam and Pdx and apparent dissociation constants (K_d^{kin}) of oxyP450cam/reduced Pdx complex were obtained from curve fitting of the eq i to the experimental data (Table 1). k_{obs} for the wild-type enzyme was larger than that for the mutants over the whole range of

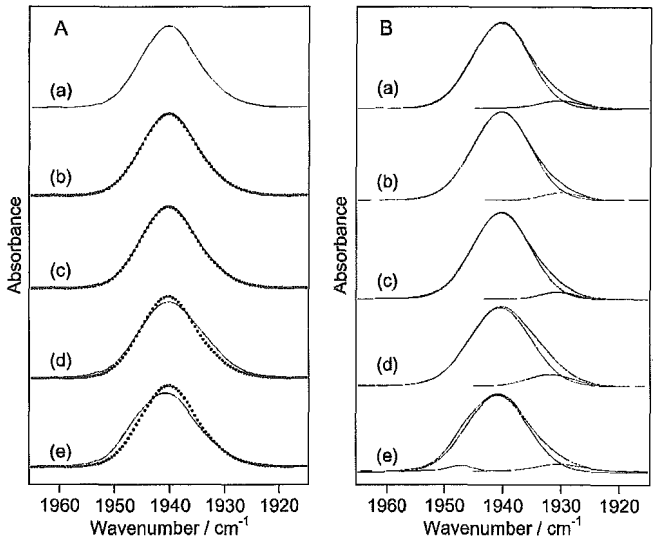

FIGURE 3: IR ν_{C-O} spectra of CO-P450cam of wild type and mutants. The spectra are 500 μM P450cam in 50 mM K phosphate buffer, pH 7.4, containing 50 mM KCl and 1 mM D-camphor and 20 °C. Traces in panel A and B are of wild type (a), R109K (b), R109Q (c), R112K (d), and R112M (e). In panel A, the wild-type spectrum is shown as dotted lines in traces b–e. Panel B shows decomposed single spectra for each spectrum. CO-P450cam was prepared as described in Experimental Procedures.

Pdx concentration examined and k_{obs} for the mutants were R109K > R112K > R109Q. In each profile, the rate constant reaches a plateau as the concentration of Pdx exceeds 20 μM for the wild-type P450cam and 80 μM for the three mutants. It is of note that R112M oxyP450cam did not decompose in the presence of 200-fold excess of reduced Pdx for over 500 ms, suggesting that the observed rate constants (k_{obs}) for R112M were less than 1% of the wild type in the whole Pdx concentration range examined. Thus, the introduction of neutral side chain at 112 drastically retarded the rate of breakdown of its oxy form. That the mutations at position 112 significantly reduced the rate for breakdown of the oxyP450cam with Pdx and its affinity for Pdx indicated that Ag112 is a critical residue required for P450cam–Pdx interaction and the monooxygenation reaction. In addition, Arg109 also turned out to be a critical residue. From the present and previous results (*20*, *26*, *27*), we conclude that Arg109 and Arg112 are the constituents of the Pdx-binding site for oxy-ferrous and ferric states of P450cam.

IR ν_{C-O} Spectra. We measured IR ν_{C-O} spectra of CO-P450cam in the absence and presence of reduced Pdx, as a stable mimic of oxyP450cam. Spectra of the wild-type enzyme and its mutant in the absence of Pdx are shown in Figure 3. The spectrum of the wild-type P450cam (trace a in Figure 3A) exhibits an almost symmetric ν_{C-O} band at 1940 cm^{-1} as reported previously (*13*, *28*, *29*). Decomposition of the spectrum into single bands revealed that, in addition to the main band at 1940 cm^{-1}, a minor band at 1932 cm^{-1} was present in the spectrum of the wild-type enzyme (trace a in Figure 3B). The main and minor bands (bands I and II, respectively) account for 95 and 5% of the entire band area. The spectra of R79Q, R109K, and R109Q mutant P450cam were almost identical to that of the wild-type enzyme (traces b and c in Figure 3A; spectrum for R79Q not shown). Decomposition of these mutant spectra also yielded two bands with the same band area and frequencies

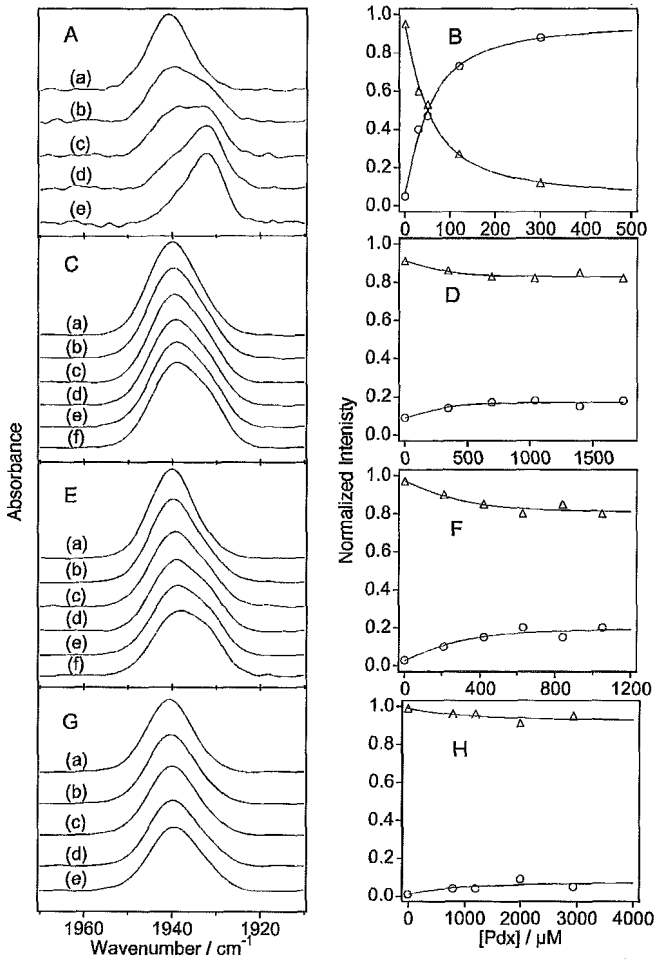

FIGURE 4: IR ν_{C-O} spectra of CO-P450cam in the presence of a varying concentration of reduced Pdx. (A) 45 μM wild-type P450cam and [Pdx] = 0 (a), 30 (b), 50 (c), 120 (d), and 300 μM (e). (C) 420 μM R112K and [Pdx] = 0 (a), 350 (b), 690 (c), 1040 (d), 1390 (e), and 1740 μM (f). (E) 320 μM R109K and [Pdx] = 0 (a), 210 (b), 420 (c), 630 (d), 840 (e), and 1050 μM (f). (G) 320 μM R109Q and [Pdx] = 0 (a), 800 (b), 1200 (c), 2000 (d), and 2940 μM (e). Changes in bands I (open triangle) and II (open circle) intensities vs [Pdx] are presented in panels B, D, F, and H for wild type, R112K, R109K, and R109Q, respectively. The other measurement conditions are as indicated for Figure 3.

as found for the wild type (traces b and c in Figure 3B; spectrum for R79Q is not shown), indicating that the mutations had little effect on the IR spectra. The mutation of Arg112 to Lys caused a slight reduction of the intensity of band I while causing a subtle broadening at the lower energy side of the band as shown in trace d of Figure 3A. These small changes were ascribed to changes in areas of bands I and II to 90 and 10%, respectively, without shifting the frequencies (trace d in Figure 3B). The R112M mutant shows more changes (trace e in Figure 3A). In addition to the bands I and II (band area = 90 and 7%, respectively), the spectrum exhibited an extra band at 1947 cm^{-1} (band area = 3%) (spectrum e in Figure 3B).

Next, we measured IR ν_{C-O} spectra of CO-P450cam in the presence of a varying concentration of Pdx. Wild-type P450cam showed spectral changes as the concentration of Pdx was raised as shown in Figure 4A. In the presence of about 3 equiv of Pdx and more, its ν_{C-O} changed to an asymmetric band centered at 1932 cm^{-1} (traces d and e in Figure 4A). Decomposition of these spectra revealed that band I decreased as the concentration of Pdx increased with a concomitant increase of band II, although the band frequencies did not shift. The areas of bands I and II were plotted as a function of Pdx concentration (Figure 4B). From the best-fitted titration curve obtained by assuming a 1:1 complex, wild-type CO-P450cam was shown to have bands I and II, which have relative intensities of 3 and 97%, respectively. The dissociation constant (K_d^{IR}) of the wild-type P450cam for reduced Pdx was determined to be 22 μM, which is in good agreement with the value derived from NMR titration (*10*, *11*) and that from current kinetic analysis (K_d^{kin} in Table 1). Decomposition of R112K spectra (Figure 4D) also revealed that band II intensity increased while band I decreased as Pdx concentration was raised. However, the change is remarkably small compared with that of the wild type (Figure 4B): CO-P450cam/Pdx complex of R112K exhibited bands I and II with relative band intensities of 80 and 20%, respectively. Analysis of the profile of the band intensity vs [Pdx] revealed that the dissociation constant of the R112K was 38 μM (Table 1). Likewise, both R109K and R109Q mutants had a less intense band II in the CO-P450cam/Pdx complex and had larger K_d^{IR} values than wild-type enzyme (Figure 4E–H and Table 1). R112M mutant showed little spectral change even in the presence of 20 equiv of reduced Pdx (spectra not shown). Hence, although all the 109 and 112 mutations decreased the binding affinity of P450cam to reduced Pdx, their most prominent effect was the remarkable decrease of the conformational change at the active site resulting from Pdx binding.

X-ray Crystal Structures. To gain further insight into the effects of mutations on the interaction between Pdx and P450cam, we analyzed the X-ray crystal structures of the wild-type, R109K, and R112K mutant enzymes at 2.0-Å resolution (Table 2 and Figure 5). The two mutant enzyme structures have overall root-mean-square differences of 0.06 and 0.16 Å, respectively, in main chain atoms from the wild-type enzyme. Such small root-mean-square differences indicate that the overall structures of the mutant proteins are essentially identical to that of the wild-type enzyme. The distal side structure including D-camphor and Thr252, which is a critical residue for a proton supply leading to O–O bond scission (*3*–*7*), is essentially unchanged by the mutations (Figure 5B,C). As found for wild type, Lys109 is projected outward away from the surface of the molecule. The R109K mutation caused no significant change at the proximal side structure. In contrast, the R112K mutation significantly altered the conformation of the loop including the proximal ligand: the backbone atoms of Leu358 moved toward the heme by 0.6 Å.

DISCUSSION

Conformational Change and Breakdown of oxyP450cam. To date, numerous spectroscopic studies have been carried out to elucidate the role of conformational changes on P450cam induced by Pdx binding. However, no quantitative evaluations have been made in terms of the relationship between the conformational changes and oxygen activation of P450cam. Current IR spectroscopic and kinetic data provide significant insight into this relationship.

Mutations at 109 and 112 notably changed intensity distribution of bands I and II of the CO-P450cam/Pdx complex. Relative band II intensities are 97, 18, 16, and 9%

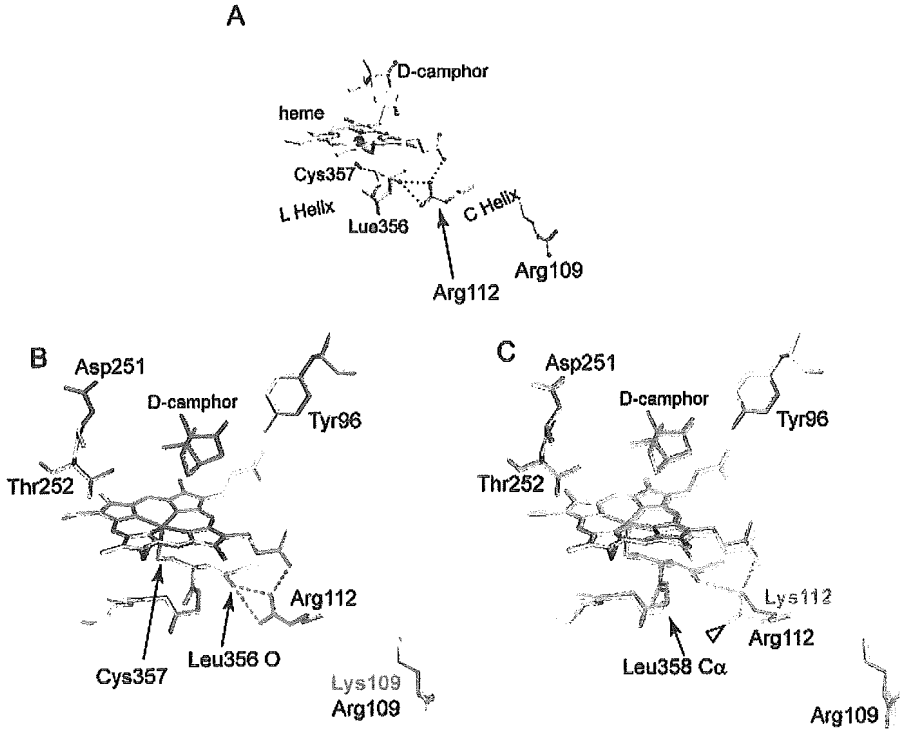

FIGURE 5: Crystal structures of ferric D-camphor-bound forms of P450cam. Panel A illustrates the active site and presumed Pdx-binding site of wild-type P450cam. The heme, D-camphor, the proximal ligand (Cys357), Leu356, Arg112, and Arg109 are shown in a yellow-colored stick model. Red, blue, brown, and green spheres represent oxygen, nitrogen, iron, and sulfur atom, respectively. Arg109 at the C helix extends toward the bulk water from the molecular surface, while Arg112 extends its side chain from the C helix toward the loop preceding the L helix forming hydrogen bonds (dashed line) with the heme 6-propionate and the main chain O atom of Leu356. Parts of the main chain are presented as a gray ribbon model. Panels B and C show the overlaid proximal side and the mutation site structures. Yellow, cyan, and green stick models show wild type, R109K, and R112K, respectively. The D-camphor, heme, main chain atoms of Leu356–Gln360, and side chains at 96, 109, 112, 251, and 252 are shown. The hydrogen bonds from Arg or Lys112 are drawn as dashed line. Open arrowhead indicates Arg112 Nη atom which is expected to hydrogen bond to Pdx. Figures were prepared by MOLSCRIPT (*40*) and RASTER3D (*41*) or PYMOL (*42*).

for the wild type, R109K, R112K, and R109Q, respectively, decreasing in the same order as in rates of decomposition (k_2) of oxyP450cam with reduced Pdx (Table 1). Furthermore, the oxy form of R112M, which does not decompose to products in the presence of a 200-fold excess of reduced Pdx over 500 ms, shows little spectral change when 20 equiv of reduced Pdx is added. These results indicate significant positive correlation between the conformational change and decomposition of the oxyP450cam/Pdx complex to products, implying that the conformational change promotes D-camphor hydroxylation by P450cam.

Enhanced Electron Donation from Proximal Ligand. ν_{C-O} and ν_{Fe-CO} can shift lower and higher, respectively, by increased back-donation from the heme iron (*30*). This inverse back-donation correlation is linear for the same proximal ligand to heme. According to the back-donation correlation of P450cam (*31*, *32*) together with 8 cm^{-1} downshift of ν_{C-O}, ν_{Fe-CO} is expected to upshift ca. 5 cm^{-1}. However, we have previously shown that ν_{Fe-CO} upshifts only 2 cm^{-1} upon Pdx binding (*33*), which is significantly smaller than the expected value. The small shift of ν_{Fe-CO} is explained in terms of enhanced electron donation from Cys ligand to the heme; the enhanced electron donation from a proximal ligand compete with σ-donation from the distal ligand, resulting in net lowering or smaller increase of ν_{Fe-CO} (*15*). Consistently, ν_{Fe-S} in ferric substrate-bound form upshifts ca. 3 cm^{-1} upon complexation with Pdx (*14*). Furthermore, NO-P450cam has two ν_{Fe-NO} bands and binding of reduced Pdx increases the intensity of the high-frequency band and decreases the low-frequency band, supporting the Pdx-binding induced increased electron donation from the proximal ligand, Cys357, to the heme iron (*15*). The enhanced electron donation from Cys357 would be caused by the alteration of the proximal side structure including Arg112 as discussed below.

Conformational Change Caused through Arg112. Arg112 extends its guanidium group to the loop preceding the L helix to form hydrogen bonds with heme propionate and the main chain carbonyl of Leu356 next to the proximal ligand. According to the model structure of the P450cam/Pdx complex reported by Pochapsky et al. (*16*), Arg112 hydrogen bonds to Pdx Asp38 that is located next to the redox center, a 2Fe-2S cluster. The critical role of the Asp38 for the interaction with P450cam is demonstrated by the lower affinity of the Asp38 → Asn mutant for P450cam (*34*). Thus, in the P450cam/Pdx complex, as we proposed previously (*35*), two metal centers interact with each other through the hydrogen bond network connected by the guanidium group of Arg112. In the R112K mutant, Lys112 is hydrogen bonded to the active center as found for Arg112 (Figure 5A,C). Although IR titration showed that R112K forms a 1:1 complex with Pdx and its overall structure was essentially unchanged, Lys112 would not be able to form a hydrogen bond with Pdx because its side chain N_ϵ atom is 2.7 Å closer to the active site (i.e., might be further away from Pdx) than the N_η of Arg112 which is expected to hydrogen bonds to

Pdx. Therefore, the amino acid substitution of Arg for Lys at 112 is expected to cause a loss or weakening of the interaction with Pdx through the side chain at 112. In fact, the mutation causes a decrease in the binding affinity toward reduced Pdx (Table 1). Furthermore, it is very interesting to note that the mutation significantly decreases the degree of the conformational change. Hence, a hydrogen bond network around Arg112 has a primary role in the conformational change. Such a role of Arg112 can also be envisaged in P450cam in the absence of Pdx as indicated by the different band II/band I ratio for wild type and 112 mutants (traces d and e in Figure 3B). On the other hand, the mutation of Arg109, which has no direct interaction with the proximal side of the heme, to Lys or Gln does not cause the conformational change in P450cam in the absence of Pdx but instead assists in the interaction between Pdx and P450cam via Arg112 by docking the two proteins in a proper orientation as shown by the limited conformational change of the 109 mutants upon Pdx binding. The 109 and 112 mutations thus alter the hydrogen bond network including Arg112, heme propionate, and proximal heme ligand, resulting in an increase in electron donation from Cys357. In fact, mutations at the proximal site, such as Leu358 → Pro and Gln360 → Leu or Pro significantly altered the hydrogen bond network around Cys357 and, subsequently, changed the electron donation properties of the proximal ligand (*36*).

As to the effects of Pdx binding on the structure of P450cam, we must also consider the previously proposed mechanism (*14*): electron donation is enhanced by shielding of positive charges by acidic residues of Pdx at the proximal face of P450cam. According to the mechanism, a mutation that removes surface positive charge is expected to cause a downshift of band I and/or increase in a ratio of band II/band I of CO-P450cam in the absence of Pdx. Contrary to this expectation, R109Q and R79Q showed neither downshift of band I nor increase of band II/band I ratio (spectrum for R79Q not shown). These results are not compatible with the mechanism, suggesting that shielding of positive charge is not a primary cause for the conformational conversion. These arguments again lead us to suggest that Pdx binding causes structural change around the proximal ligand through Arg112, resulting in changes of various spectroscopic properties including current IR data. Consistently, the R112K mutation, which altered the conformation of the proximal side loop including Cys356, increased the band II/band I ratio.

Significance on Oxygen Activation. Similar to the results obtained with CO-P450cam, an increase in a lower ν_{O-O} band and concomitant decreases in higher ν_{O-O} bands upon complexation with Pdx have been reported (*32*). Another similar spectral change is that the inverse correlation does not apply to ν_{Fe-XO}/ν_{X-O} (X = C or O) of both CO-P450cam and oxyP450cam. This unusual relationship would be explained by an enhanced electron donation from the proximal ligand and a σ-competition effect (*15*) as discussed above. These similar spectroscopic properties indicated that essentially the same conformational change is taking place upon Pdx binding irrespective of the ligand bound to ferrous P450cam. These arguments allow us to discuss how oxygen activation by P450cam is promoted by the conformational change.

As already mentioned, Pdx-binding changes the proximal side hydrogen bond network by interactions via Arg112, resulting in enhanced electron donation from the proximal ligand to the heme iron. The enhanced electron donation increases electron density in the $d\pi$(Fe) orbital and the π-back-donation from the iron to O_2 ligand, which facilitates cleavage of O−O bond to give an active oxygen species, oxo-ferryl π-cation radical species called compound I. Similar enhancement of O−O bond scission is also observed for the mutant P450cam, L358P, which has shown to have stronger electron donation than wild type in the absence of Pdx (*36*, *37*).

It has recently been proposed that the Pdx binding induced conformational changes prevent uncoupling of oxygen consumption to the substrate hydroxylation by enforcing a conformation of P450cam that prevents loss of substrate and/or intermediates prior to turnover (*10*) or by relocation of D-camphor closer to the reactive oxygen atom of compound I (*11*). However, the 109 and 112 mutants, which all showed very limited conformational change, utilized almost all the oxygen consumed to hydroxylate D-camphor as wild type. Therefore, contrary to their proposal, IR detectable conformational change is not related with the coupling of dioxygen reduction to the substrate monooxygenation although the current data do not preclude the occurrence of the structural change at the distal site.

In the breakdown of oxyP450cam, electron transfer is one of the critical steps. It is possible that Pdx binding modulates the redox potentials of the two metal centers, thereby changing the electron-transfer rate. However, as already mentioned, two other iron−sulfur proteins, beef adrenodoxin and spinach ferredoxin, which have lower redox potentials than Pdx, cannot donate an electron to oxyP450cam to yield the reaction products (*8*). Therefore, it is less likely that the change of the redox potential induced by Pdx binding, if any, promotes breakdown of oxyP450cam. On the other hand, electronic coupling and/or reorganization energy, which are other critical parameters for electron-transfer rate, could be changed as follows.

We have already reported that EPR spectra of reduced Pdx also changed upon binding of CO-, NO-, or O_2-bound P450cam, suggesting that the structure around the 2Fe-2S cluster is changed by hexacoordinated P450cam binding (*35*). The 109 and 112 mutants, as found for IR spectroscopy, also show less spectral changes. Therefore, the conformation of intervening residues and, possibly, water molecule(s) (*38*) between the two metal centers changed simultaneously upon complex formation. It is of interest to note that the mutations at 112 drastically decelerate the electron transfer from reduced Pdx to ferric P450cam (*20*). It would thus be possible that the conformational change modulates an electronic coupling between the two metal centers as shown in Zn cytochrome *c*/plastcyanin complex (*39*) or reorganization energy to increase the electron-transfer rate.

Conclusions. We have found significant positive correlation between the Pdx-induced conformational change of CO-P450cam and the breakdown rates of oxyP450cam/Pdx complex to give the reaction products. Contrary to the previously proposed role of the conformational change, no significant relationship between the conformational change and the coupling ratio was observed. Pdx binding would modulate the conformation of the intervening residues between the two metal centers through Arg112, resulting in the enhancement of electron donation from the proximal